#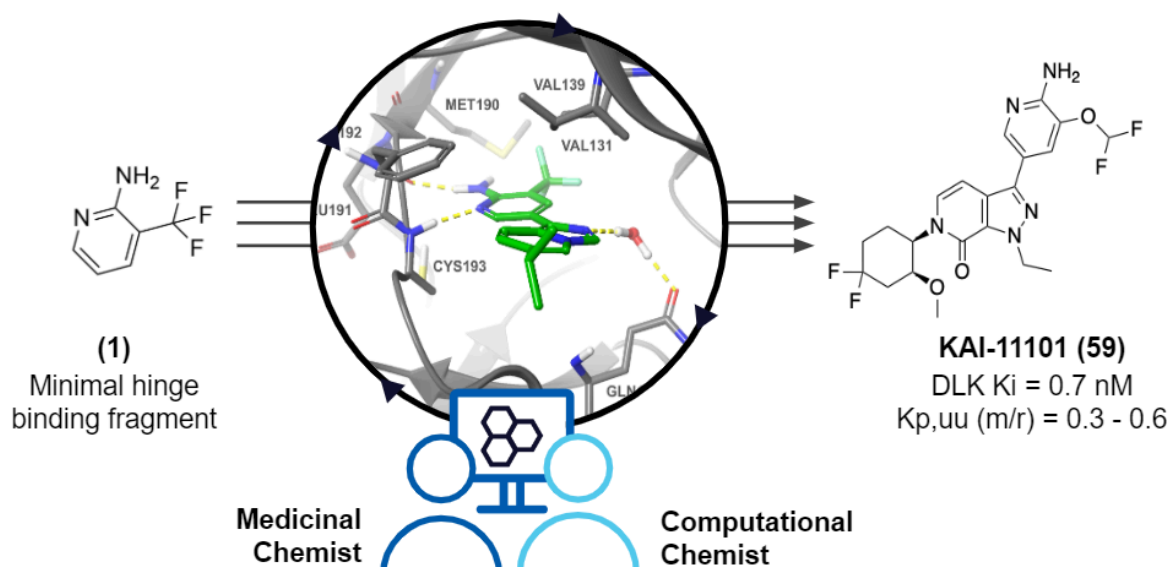 In Silico Enabled Discovery of KAI-11101, a Preclinical DLK Inhibitor for the Treatment of Neurodegenerative Disease and Neuronal Injury

H. Rachel Lagiakos*, Yefen Zou, Hideyuki Igawa, Eric Therrien, Morgan Lawrenz, Mitsunori Kato, Mats Svensson, Felicia Gray, Kristian K. Jensen, Markus K. Dahlgren, Robert D. Pelletier, Karen H. Dingley, Jeffrey A. Bell, Yuansong Jiang, Hua Zhou, Robert J. Skene, and Zhe Nie*

ABSTRACT

Dual leucine zipper kinase (DLK), expressed primarily in neuronal cells, is a regulator of neuronal degeneration in response to cellular stress from chronic disease or neuronal injury. This makes it an attractive target for the treatment of neurodegenerative diseases such as Alzheimer's, Parkinson's, and amyotrophic lateral sclerosis; and neuronal injury, such as chemotherapy induced peripheral neuropathy. Here we describe the discovery of a potent, selective, brain-penetrant DLK inhibitor, KAI-11101 (**59**). Throughout the program's progression, medicinal chemistry challenges such as potency, hERG inhibition, CNS penetration, CYP3A time-dependent inhibition, and kinase selectivity were overcome through the implementation of cutting-edge *in silico* tools. KAI-11101 displayed an excellent *in vitro* safety profile and showed neuroprotective properties in an *ex vivo* axon fragmentation assay as well as dose-dependent activity in a mouse PD model.

(1)
Minimal hinge binding fragment

KAI-11101 (59)
DLK Ki = 0.7 nM
Kp,uu (m/r) = 0.3 - 0.6

Medicinal Chemist

Computational Chemist

INTRODUCTION

Axon degeneration is prevalent in neurodegenerative diseases of the central and peripheral nervous systems, contributing to disease progression and disability in chronic diseases such as Parkinson's disease, amyotrophic lateral sclerosis (ALS) and acute conditions such as traumatic brain injury or chemotherapy induced peripheral neuropathy (CIPN). CIPN is a common disorder caused by multiple chemotherapies. CIPN presentation can include neuropathic pain, numbness of distal extremities and sensitivity to thermal changes. There are currently no effective treatment options for CIPN and while an understanding of the complete mechanism of CIPN is evolving, there is evidence that axon degeneration of distal nerve endings is a driver of this pathology.[1] Novel therapeutics to preserve axons may reduce CIPN morbidity for cancer patients.

Dual leucine zipper kinase (DLK, also known as MAP3K12) is a member of the mixed lineage kinase (MLK) family that contains an N-terminal kinase domain followed by two leucine zipper domains and a glycine/serine/proline rich C-terminal domain. It is expressed primarily in neuronal cells, specifically in the synaptic terminal and axon of neurons. Injury to axons or other cellular stress leads to DLK dimerization, autophosphorylation, phosphorylation of MKK7 and JNK/cJun pathway activation.[2] Recent work has demonstrated that genetic deletion or pharmacological inhibition of DLK results in attenuation of synapse loss, neuronal degeneration, and functional decline in models of both Alzheimer's disease and ALS[3–5] as well as protection from CIPN in preclinical models.[6,7] Based on these findings, DLK inhibition is proposed to provide functional protection in the context of injuries or diseases characterized by axonal degeneration, making DLK an attractive therapeutic target for the treatment of conditions such

as ALS and CIPN.[8] Given the unmet medical need, we sought to develop a potent, selective and CNS-penetrant DLK inhibitor suitable for the treatment of these neurodegenerative indications.

DLK inhibition activity of several marketed and clinical kinase inhibitors was first reported in 2008 to highlight the feasibility of inhibiting DLK as an attractive therapeutic target.[9,10] However, lack of selectivity and efficient CNS penetration of these early inhibitors prevented them from being used as tool compounds to interrogate DLK biology. Since then, efforts to discover a selective and CNS penetrant DLK inhibitor have resulted in several patents and primary literature from Genentech/Roche, Denali Therapeutics and Magnolia Neuroscience/University of Texas (Figure 1). From Genentech, **GNE-3511** was the first potent and selective DLK inhibitor reported with good CNS penetration and *in vivo* efficacy.[11] Next Genentech published **GNE cpd 10**, a tool asset where the liganded DLK crystal structure (PDB:5VO1) helped enable structure-based design,[3] and finally, their clinical asset, **GDC-0134**, which has completed a phase 1 trial in patients with ALS.[12] In 2022, Denali published the structurally related amino pyrazine **DN-1289** which showed target and pathway modulation in an *in vivo* model of ALS,[5] and in 2023, Magnolia Neuroscience/University of Texas disclosed imidazole derivative **IACS-52825** that displayed potent, selective DLK inhibition and showed favorable *in vivo* efficacy in a mouse model of chemotherapy-induced peripheral neuropathy (CIPN).[6]
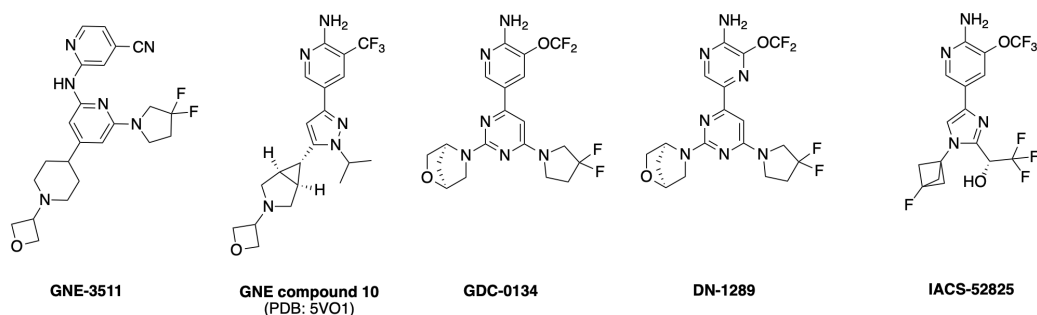
Figure 1. Representative structures of publicly disclosed DLK inhibitors.

RESULTS

Hit finding strategy. Free energy perturbation (FEP) is a computational technique using molecular dynamics simulations to calculate the protein-ligand binding free energy with a precision that rivals experimental methods.[13,14] This powerful approach enables prediction of the affinity of a compound before synthesis, which inturn enables the project team to focus their time and resources preparing compounds that are more likely to be potent binders. We leveraged this *in silico* tool extensively as we initiated our hit finding campaign.

As we began our discovery campaign, we were drawn to the known 3-trifluoromethyl-2-aminopyridine motif (**1**) as a ligand efficient, minimal hinge binding fragment. We then took a stepwise, *in silico*-driven approach whereby cores and R-groups were enumerated sequentially and scored using FEP (Figure 2). This allowed for significant structural diversity to be rapidly surveyed computationally. At each step, a small set of representative molecules were synthesized and tested to facilitate the subsequent design cycle; provide relevant FEP references for each iterative modeling cycle; and most importantly, validate model

performance. Once suitable cores were identified, multiple chemical series were further refined through iterative optimizations.
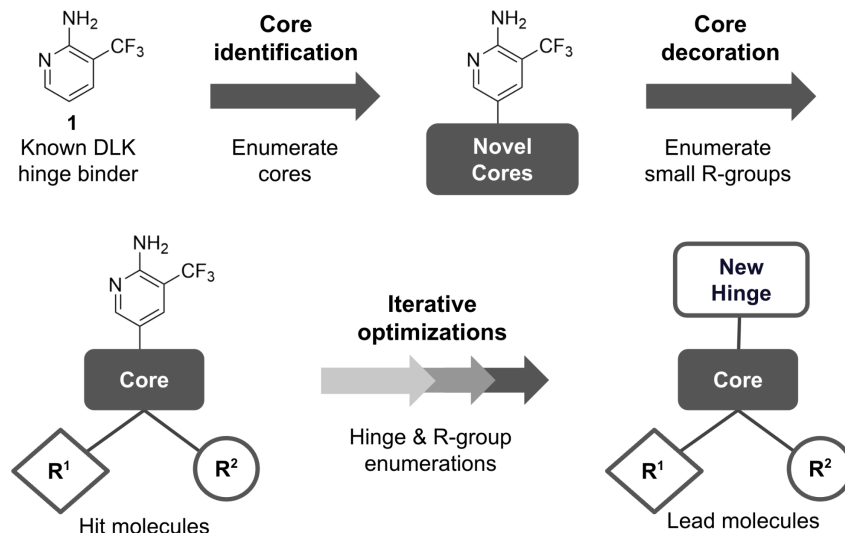

Figure 2. FEP-driven stepwise approach for hit identification.

With fragment **1** as a starting point, approximately 800 unsubstituted heteroaromatic cores (monocyclic and bicyclic) were enumerated and evaluated by FEP using an available DLK co-crystal structure.[3] As illustrated in Figure 3, enumerating the cores at each available position generated approximately 2400 new ideas, which were further filtered using docking to eliminate potential clashes with the protein. We then used single edge FEP with a short simulation time to efficiently profile this large set of ideas. After rank ordering of the predictions and manual selection, a set of 47 ideas were further profiled using full cycle closure FEP.
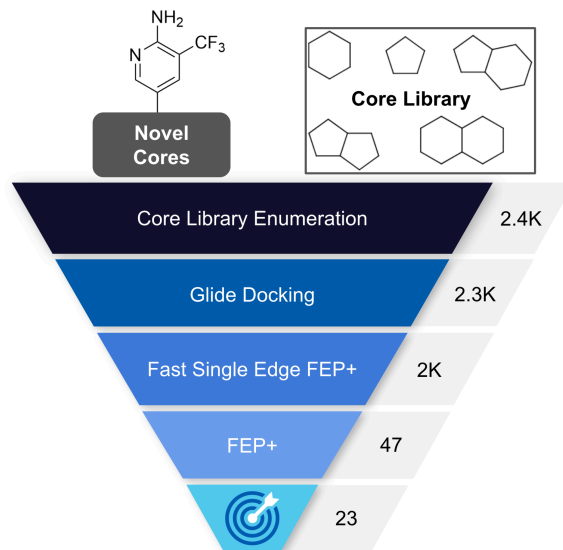
Figure 3. Core identification approach using FEP.

From this work, a diverse set of 23 synthetically tractable, unsubstituted cores were prioritized for synthesis. Table 1 shows a selection of representative examples, all of which were confirmed to be DLK inhibitors. The compounds were potent (ranging from IC_{50} of 63 - 420 nM), ligand efficient (LE 0.45 - 0.53), low molecular weight (<300), with CNS pMPO scores of 0.6 - 0.9 suggesting these compounds would have a higher probability of being brain penetrant.[15] Importantly this first round allowed us to establish the relationship between our predictions and experimental readout. FEP predicted binding affinities correlated well with DLK biochemical inhibition data, giving us the confidence to continue utilizing FEP- guided iterations to elaborate these attractive starting points further.

Table 1. Initial novel DLK inhibitor cores identified by FEP.
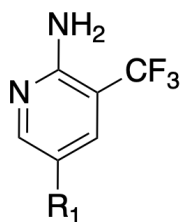
Cmpd	R$_1$	FEP Predicted K$_i$ (nM)	DLK K$_i$ (nM)	LE	Molecular Weight	Merck CNS pMPO
2		342	421.1	0.45	279	0.63
3		159	63.3	0.52	278	0.86
4		88	148.9	0.48	279	0.76
5		181	194.5	0.47	278	0.84
6		44	72.4	0.53	284	0.85
7		113	416	0.45	296	0.82

Further core decoration using a set of 42-member small R-group library consisting of 1-4 atom substituents (e.g. Me, iPr, CN, OCF$_3$, NHMe and oxetane) allowed us to evaluate every available position on each core system *in silico*. Around 1000 total ideas were enumerated and 686 ideas evaluated by FEP. Figure 4 shows the distribution of FEP predicted binding affinities for the decorated cores.
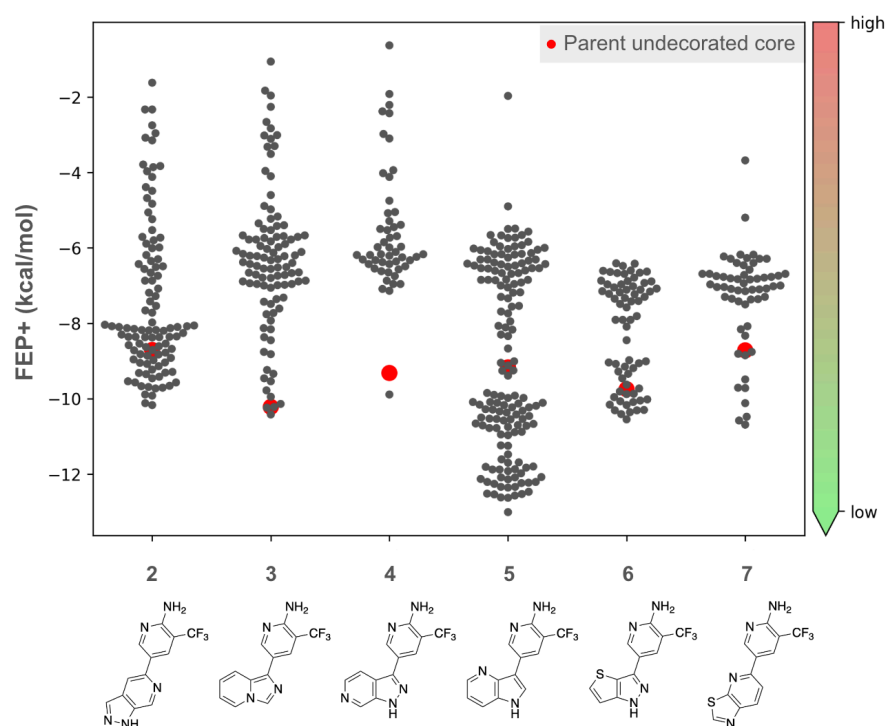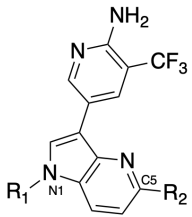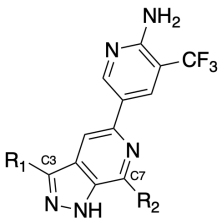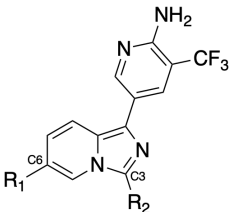

Figure 4. FEP predicted binding affinities for decorated cores. The red dots represent the experimental DLK biochemical activity (kcal/mol) of the parent undecorated core while the black dots represent the predicted binding affinity of derivatives using FEP.

In Table 2, we show three cores which were prioritized based on predicted potencies, synthetic feasibility, and the amenability of the core to allow for diverse SAR explorations across a number of different vectors. The small R-group enumeration activity allowed us to rapidly hone in on the positions most amenable to substitution. For the pyrrolopyridine core, the N1 (**8**) and C5 (**9**) positions were predicted by FEP to be favorable for substitution; for the pyrazolopyridine

core, C3 (**11**) and C7 (**10**) positions; and for the imidazopyridine core, C3 (**13**) and C6 (**12**)

positions. These small substitutions had a rapid impact, improving potency over the

unsubstituted parent scaffold (5 - 60 fold) and maintaining ligand efficiencies. In the case of the

imidazopyridine core, single digit nanomolar potency was achieved after only a few short SAR

cycles (**13**). Importantly, FEP predicted binding affinities continued to correlate well with

experimentally measured inhibition data.

Table 2. Small R-group enumeration exemplars.

Cmpd	Series	R_1	R_2	FEP Predicted K_i (nM)	DLK K_i (nM)	LE
5		H	H	181	194	0.47
8		cBu	H	12	27	0.44
9		i-Pr	cPr	4	59	0.39
2		H	H	342	421	0.45
10		H	cPr	92	61	0.44
11		i-Pr	H	106	79	0.43
3		H	H	159	63	0.52
12		i-Pr	H	51	12	0.49
13		oxetane	Et	14	1[a]	0.48

[a]ATP concentration of 500 μM used instead of 100 μM for other compounds in the table.

Hit to Lead on Imidazopyridine series. Whilst initially exploring these three series in parallel,

after a few rounds of ideation, FEP evaluation, synthesis, biological testing and ADME/PK

profiling, the imidazopyridine series was determined to be the most promising chemical series given its potent DLK inhibition and favorable oral PK (Tables 3 and 5). For example, analog **12** was rapidly identified as a potent and highly ligand efficient DLK inhibitor (DLK K_i= 12 nM, LE = 0.48) with a modest cellular potency (pJNK cell IC_{50} = 490 nM). A co-crystal structure of human DLK with **12** was solved and confirmed the binding mode at the kinase domain (Figure 5). The amino-pyridine hinge binder interacts through H-bonds with the backbone of the residues GLU191 and CYS193. The pyridine ring from the imidazopyridine is positioned closer to the hinge binding groove where an edge-on π-stacking interaction with PHE192 might be responsible for its enhanced binding affinity. The isopropyl substitution makes additional hydrophobic contacts with the adjacent protein residues and points toward the solvent exposed region. The imidazolo nitrogen forms a water bridged interaction with GLN197.
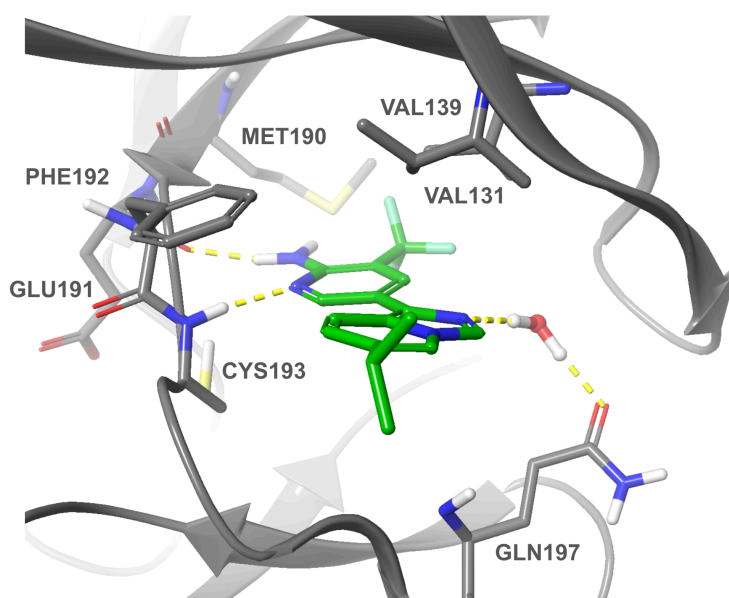

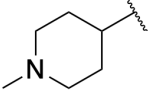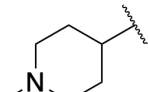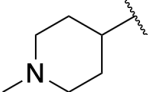**Figure 5**. Co-crystal structure of human DLK with **12**. Only key residues are shown for clarity.

The co-crystal structure pointed out opportunities to interact with P-loop via substitution on the imidazolo C3 position and also adding solubilizing groups to adjust physicochemical properties

at C6 position. Thus, initial SAR exploration of the imidazopyridine series was focused on the C3 and C6 positions of the imidazopyridine ring.

For C6 substitutions, library enumerations were complemented with rational designs. The top compounds with good predicted DLK inhibitory potency by FEP were selected for synthesis. As shown in Table 3, as compared to experimental DLK K_i values of the synthesized compounds, all of the FEP predictions were within 5-fold accuracy. Replacing the lipophilic *i*-Pr group of example (**12**) with the more polar oxetanyl piperidine (**14**), allowed for a ~4-fold improvement to both biochemical and cellular potency. Installing basic groups at C6 position (examples **15-17**) was beneficial to potency. Example **17**, which contains an *N*-methylpiperidine-4-yl solvent exposed group is a potent DLK inhibitor (DLK K_i=1.5 nM and p-JNK cell IC_{50}=128 nM), and this motif, given its favorable potency was used as an anchor as we explored the C3 position. For C3 substitutions, adding small alkyl substitutions, such as an ethyl (**18**) or the more polar heterocyclic THF ring (**22**), improved potency by almost 5-fold in both our biochemical and cellular assays. Again, FEP predicted K_i values continued to agree well with the experimental K_i values. Both the C6 and C3 positions proved quite amenable to diverse substitutions and can be utilized in the future as handles for modulation of physicochemical properties.

Table 3. Imidazopyridine series SAR.
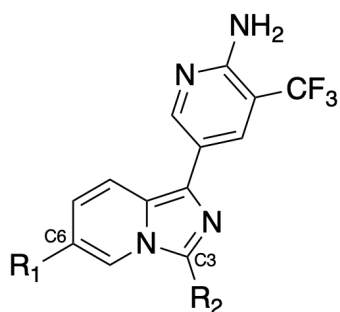
Cmpd	R_1	R_2	FEP Predicted K_i (nM)	DLK K_i (nM)	p-JNK cell IC_{50} (nM)	LE
12	i-Pr	H	51	9.2	490	0.48
14		H	2.1	3.2	134	0.39
15		H	4.5	4.5	405	0.41
16		H	2.9	4.3	90	0.44
17		H	9.0	1.5	128	0.46
18		Et	1.1	0.3	23	0.46
19		CN	6.1	4.8	162	0.39

20		CF₃	10.6	2.1	94	0.39
21			2.0	1.2	54	0.42
22			0.6	0.7	22	0.41
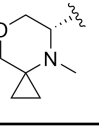
From this set, compound **18** emerged as an attractive DLK inhibitor. It was potent in our biochemical and cell assays (DLK K_i of 0.3 nM and pJNK cell IC_{50} of 23 nM), highly soluble (Kin Sol at pH 6.8 270 µM), stable in human liver microsomes (CLint 3 µL/min/mg), highly permeable and not a P-gp substrate (MDCK-MDR1 A-B Papp 11 x10^{-6}cm/s; ER 1.6). *In vivo* mouse PK studies showed excellent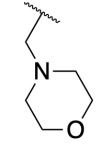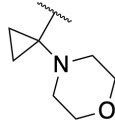 oral bioavailability (%F = 85) and a workable $K_{p,uu}$ of 0.2 (based on AUC) (Table 5). Despite those favorable properties, unfortunately, **18** showed strong inhibition in a manual patch-clamp hERG assay (hERG IC_{50} < 0.4 µM) and further progression of this ligand was halted.

To reduce hERG inhibition in our follow up analogues, several common strategies were attempted, including reducing LogD, increasing three dimensionality, modulating basicity, or combinations of the three. As shown in Table 4, adding polar groups or increasing three dimensional shape did not reduce hERG inhibition significantly (**21** and **22**). Next we tried to modulate pK_a of the basic amine functionality. Using Jaguar pK_a calculations, we prioritized the synthesis of examples where the basicity was predicted to be lowered.[16,17]

Table 4. Mitigating the hERG liability in the imidazopyridine series.
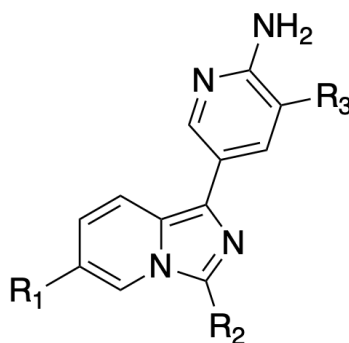
Cmpd	R$_1$	R$_2$	R$_3$	FEP Predicted K$_i$ (nM)	DLK (nM)	p-JNK cell IC$_{50}$ (nM)	logD	Jaguar pK$_a$	Exp pK$_a$	hERG IC$_{50}$ (µM)
18	*N-methylpiperidin-4-yl*	Et	CF$_3$	1.1	0.3	23	2.8	9	9.2	<0.4
21	*N-methylpiperidin-4-yl*	*1-methoxyethyl*	CF$_3$	2.0	1.2	54	2.3	8.8	-	1.3
22	*N-methylpiperidin-4-ylmethyl*	*tetrahydrofuran-2-yl*	CF$_3$	0.6	0.7	22	2.2[a]	8.8	-	0.8
23	*4-fluoro-N-methylpiperidin-4-yl*	Et	CF$_3$	0.8	0.6	40	3.6	8.0	8.4	0.6
16	*N-methylpiperidin-2-yl*	H	CF$_3$	2.9	4.3	90	3.0	7.6	8.1	1.1
24	*N-methylmorpholin-2-yl*	Et	CF$_3$	3.4	2.5	100	3.3[a]	7.4	6.8	6.9

25		Et	CF$_3$	3.6	4.6	242	3.9	7.1	6.1	2.5
26		Et	OCF$_3$	1.8	0.8	53	3.1	6.3	5.8	16
27		Et	CF$_3$	0.5	0.7	31	3.8[a]	5.0	5.1	17
28		Et	OCF$_3$	1.8	1.2	104	4.4	4.0	-	30

[a]Calculated logD (pH 7.4)

From Table 4, we can see the strong correlation between Jaguar pK$_a$ predictions and experimental measurements. Secondly, we can see the direct attenuation of hERG inhibition as the pK$_a$ of the molecule is modulated. To start, the pK$_a$ of the basic nitrogen was reduced slightly by adding a heteroatom on the piperidine ring (**23**) or moving the nitrogen closer to the bicyclic ring (**16**), though neither change was enough to significantly improve the hERG profile. Further reducing basicity to the neutral range, compounds **24-26** show much improved hERG profiles; unsurprisingly, isomeric morpholino analog **24**, which is slightly more basic than **26**, inhibits the hERG channel more strongly. Examples **27** and **28** show the lowest potential to inhibit hERG as the cyclopropyl group installs sp^2 characteristics further reducing the basicity of the morpholine nitrogen.

Through this set of compounds we became confident that we had identified the solution to mitigating hERG through the modulation of basicity, and that we could accurately predict pK$_a$.[16,17] With this data in hand, we then correlated pK$_a$ with hERG IC$_{50}$ finding that a pK$_a$ < 6.5 showed a

higher probability of having hERG IC_{50} >10 µM (Figure 6). This predictive cutoff was applied as a criteria for all future targets selected for synthesis.
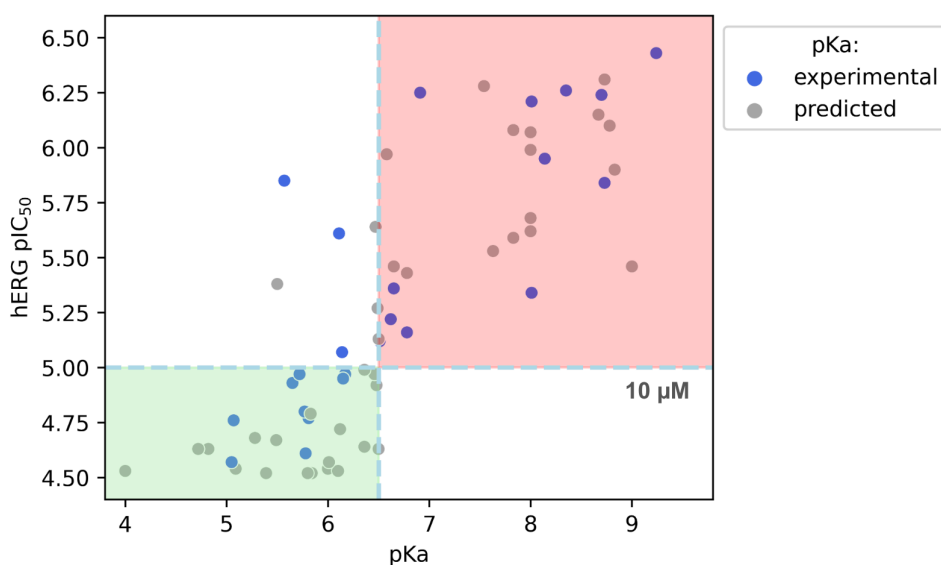

Figure 6. hERG pIC_{50} vs pK_a. Using a pK_a threshold of 6.5 predicts hERG pIC_{50} < 5 (or IC_{50} > 10 µM) with 90% accuracy and high statistical significance.

Looking at the *in vitro* ADME properties including MDCK-MDR1 permeability/efflux, human and mouse liver microsomal stability and kinetic solubility (Table 5), the majority of the compounds evaluated in the imidazopyridine series were BCS Class I compounds with high aqueous solubility and high permeability. The exception is the introduction of a completely neutral solvent exposed THP group (**29)**, which had poor kinetic solubility and showed higher turnover in human liver microsomes. Interestingly, the introduction of the OCF_2H (**31**) or OCF_3 (**26**) substituent on the aminopyridine hinge binder was influential, showing improved HLM stability as compared to the CF_3 parent (**30**). Compounds with favorable permeability, microsomal stability and kinetic solubility values were selected for mouse *in vivo* PK studies in male CD1 mice (IV 1mpk and PO 5mpk). In general, the *in vivo* mouse PK profiles of this series showed moderate to high plasma clearance (>50% Qh), short to moderate half lives (0.3 - 3.8 h), and

favorable oral bioavailabilities (%F = >85). The CNS MPO scores were quite favorable for these compounds, suggesting that they would have a higher probability of brain penetration; the resulting $K_{p,uu}$ values were workable though left room for improvement (0.14 - 0.18) (Table 5).

Table 5. In vitro and in vivo ADME properties of imidazopyridine series exemplars.[a]
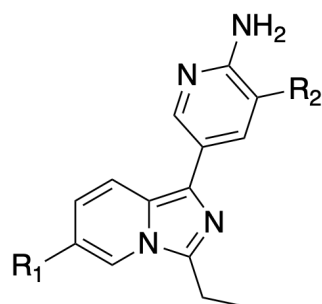
Cmpd	R₁	R₂	MDCK -MDR1 (A→B) (10^{-6} cm/s))	MDCK -MDR1 Efflux Ratio	MLM / HLM CLint (µL/min /mg)	Sol. pH 6.8 (µM)	*In vivo* Cl (mL/min /kg)	$T_{1/2}$ (h)	F (%)[b]	CNS pMPO	$K_{p,uu}$ (mouse)
18	*N-methylpiperidine*	CF_3	10.6	1.6	15 / 3	268	43	3.8	85	0.90	0.18
29	*tetrahydropyran*	CF_3	12.3	0.8	9 /27	1	-	-	-	0.74	-
30	*N-methylmorpholine*	CF_3	16.2	1.0	20 / 18	320	68	0.6	112	0.73	0.17
31	*N-methylmorpholine*	OCF_2H	30.1	0.8	17 / 8	284	109	0.3	144	0.67	0.14
26	*N-methylmorpholine*	OCF_3	37.6	0.7	11 / 6	295	40	0.8	141	0.61	0.17

[a]Mouse plasma/brain PK (PO 5mpk). [b]Saturation of clearance was observed for mouse oral bioavailability values >100.

Compound **26** presented itself as an attractive ligand, with a potent DLK K_i of 0.8 nM (FEP K_i = 1.8 nM), 48 nM p-JNK cell IC_{50}, attractive kinetic solubility (300 µM), low intrinsic clearance (MLM/HLM CLint 11/6 µL/min/mg), high permeability (MDCK-MDR1 A→B Papp 38 x 10^{-6} cm/s; ER 0.7), and a hERG IC_{50} of 16 µM. Mouse PK showed the compound to be orally bioavailable (%F = 100) and brain penetrant ($K_{p,uu}$ 0.2 based on AUC).

To show target engagement and phenotypic protection, an *ex vivo* mouse model was employed using dorsal root ganglion (DRG) neurons.[18] In this assay, neuronal cells derived from DRGs isolated from mouse embryos are cultured for 5 days to allow axons to form. In a model for CIPN, axon degeneration is induced by treatment with the chemotherapy drug paclitaxel and protection from axon degeneration is evaluated with DLK inhibitor treatment. Figure 7A shows representative images of control neurons (no treatment), neurons with axon fragmentation induced by 120 nM paclitaxel and protection by compound **26**. Quantitation of axon protection in this assay yields axon protection EC_{50} of 305 nM for **26**, which compares well to p-JNK cell IC_{50} of 48 nM (Figure 7B).
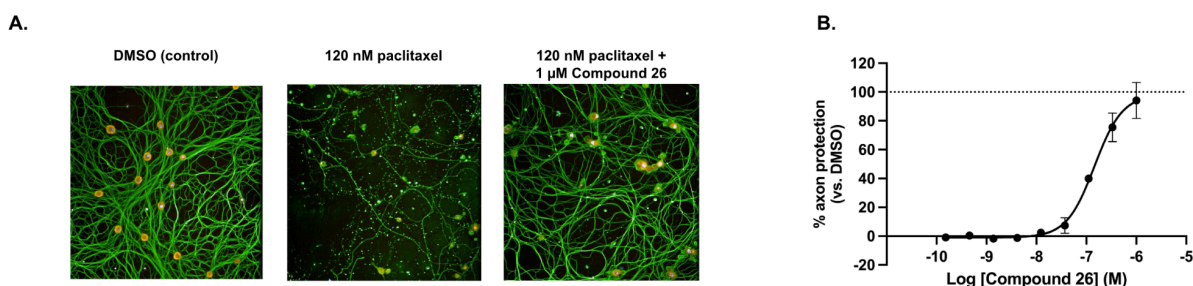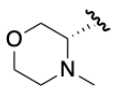

Figure 7. **A**. Representative high content images of cultured primary mouse dorsal root ganglion neurons including DMSO-treated control neurons and paclitaxel-treated neurons in the presence or absence of 1 µM compound **26** which prevented axon degeneration (images taken 72 hours after paclitaxel treatment). **B**. Axon degeneration was quantified by automated script-based image analysis and percentage axon protection relative to untreated controls was
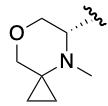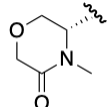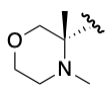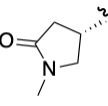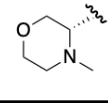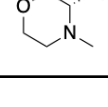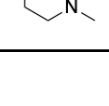
evaluated with **26** titrations. Dose response curve shows mean with SEM of three technical replicates; EC_{50} = 305 nM.

Despite showing target engagement, unfortunately, **26** and a few close analogs show time-dependent inhibition (TDI) of CYP3A as indicated in a single concentration CYP3A inhibition assay (Table 6). With 30 min pre-incubation, **26** shows 72% increased inhibition in the presence of NADPH compared to without NADPH at 30 µM. This was further evaluated by determining K_I/k_{inact} in human liver microsomes (K_I 12.4 µM, k_{inact} 0.068 min^{-1}), which might result in a potential DDI risk in the clinic based on the exposure at predicted human efficacious dose. Metabolite identification, coupled with GSH trapping experiments, identified the potential sites of reactive metabolite formation including the tertiary amine on the morpholine, the aminopyridine and the ethylimidazole.[19–21]

Table 6. Imidazopyridine series CYP3A TDI SAR.
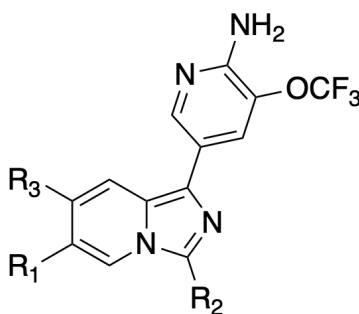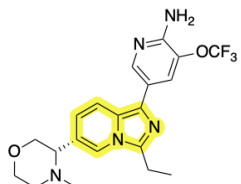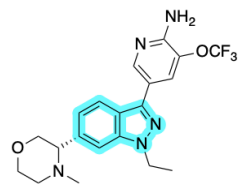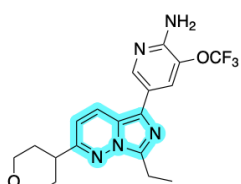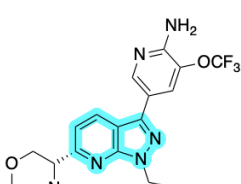
Cmpd	R_1	R_2	R_3	FEP Predicted K_i (nM)	DLK K_i (nM)	p-JNK cell IC_{50} (nM)	CYP3A TDI % Δ at 30 µM (30 min, +/- NADPH)
26		Et	H	1.8	0.8	48	72
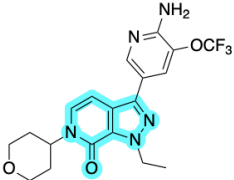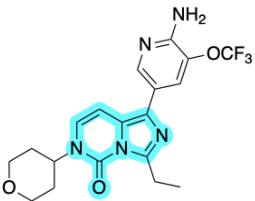
28	(structure)	Et	H	1.8	1.2	104	67
32	(structure)	Et	H	na	0.26	33	65
33	(structure)	Et	H	1.4	0.47	29	62
34	(structure)	Et	H	1.2	0.77	70	81
35	(structure)	Et	Me	2.5	5.3	290	70
36	(structure)	Et	Cl	1.9	7.1	450	67
37	(structure)	CF₃	H	8.0	3.5	300	33

Multiple strategies were explored to reduce CYP3A TDI on the imidazopyridine series as shown in Table 6. Blocking the identified sites of metabolism on the morpholine ring on either side of the tertiary amine (**28**, **32** and **33**) was not effective in reducing CYP3A TDI, nor was replacing the morpholine ring entirely with a pyrrolidinone (**34**). To block the potential epoxide formation on the pyridine ring of the imidazopyridine core, substitution of the 7-position was attempted with a Me or Cl substitution (**35** and **36**), however, both compounds did not show reduced CYP3A TDI. Substitution of the 8-position was not attempted as this position was predicted to be unfavorable for binding affinity based on FEP predictions. Finally, when the ethyl group on the imidazole ring was replaced by CF_3 (**37**), which blocks the possibility of forming an imidazolomethide, CYP3A TDI was significantly reduced *vs*. parent compound **26** (33% vs. 72%

Δ CYP3A TDI). This was quite encouraging, however, the cellular potency of **37** dropped significantly. Overall, it was quite challenging to reduce CYP3A TDI while balancing the potency and ADME properties of the imidazopyridine series.

Table 7. CYP3A TDI SAR for a set of *de novo* designed bicyclic cores.

Cmpd	Chemical Structure	FEP Predicted K_i (nM)	DLK K_i (nM)	p-JNK cell IC_{50} (nM)	CYP3A TDI % Δ at 30 μM (30 min, +/- NADPH)
26		1.8	0.8	48	72
38		8.3	1.2	103	15
39		1.7	1.6	84	78
40		3.1	2.4	94	14

Cmpd	Chemical Structure	FEP Predicted K_i (nM)	DLK K_i (nM)	p-JNK cell IC_{50} (nM)	CYP3A TDI % Δ at 30 μM (30 min, +/- NADPH)
41		4.6	2.8	110	18
42		1.3	2.0	190	87

Realizing the liability of the imidazopyridine core, an FEP-guided *de novo* core design was carried out with the goal of changing the electronics of the 5-6 bicyclic core system whilst maintaining DLK inhibition potency. As shown in Table 7, several bicyclic core systems showing potent FEP predicted DLK inhibition were prioritized for synthesis. Upon synthesizing these compounds, all of them indeed showed potent DLK inhibition. Among these, indazole **38**, azaindazole **40** and pyrazolopyridinone **41** were CYP3A TDI negative (<20% Δ CYP3A TDI at 30 μM). Beyond the favorable TDI profile, the pyrazolopyridinone **41** was potent with a good *in vitro* ADME profile (Table 9), and thus selected for further development.

Lead Optimization on the pyrazolopyridinone series. A key challenge for any CNS kinase drug discovery project is to achieve adequate brain penetration in order to ensure target engagement, demonstrate efficacy, and achieve favorable safety margins. Up to this stage of the program, we had utilized widely recognized CNS prediction metrics to inform our design process, including Pfizer CNS MPO,[22] Merck CNS MPO,[15] PSA, and MW. We also employed

MDCK-MDR1 *in vitro* screening to eliminate compounds that are P-gp substrates (MDCK-MDR1 ER > 2) before advancing them to *in vivo* PK experiments. We then utilized *in vivo* cassette or discrete rodent brain PK experiments to identify brain-penetrant compounds using the unbound brain-to-plasma drug partition coefficient $K_{p,uu}$.[23,24] Upon collecting *in vivo* $K_{p,uu}$ data, we discovered that there was no significant correlation observed with any of the commonly used metrics (Figure 8).

Figure 8. Lack of correlation of common metrics with $K_{p,uu}$. A total of 53 $K_{p,uu}$ data-points are plotted in log-scale (y-axis) with calculated metrics Pfizer MPO, Merck pMPO, Schrödinger Ralph Russ canine kidney cells (RRCK) predictions,[25] polar surface area (PSA), and measured LogD and efflux ratio from MDCK-MDR1 cell permeability assay. A target favorable $K_{p,uu}$ of 0.3 with a horizontal line is specified on each plot.

We endeavored to develop a more predictive model to drive our decision making. Analyzing in-house and public datasets of rodent brain PK data led to the identification of E-sol (energy of solvation) which showed a strong correlation to brain $K_{p,uu}$.[26] E-sol is a quantum mechanics (QM) calculation of a ligand property that models the partition between water and vacuum phases. It factors in 3D molecular conformation, size effects, the partition between gas and water, polarity,

and the energy of neutralization (pK_a) of a ligand, capturing many of the inherent properties that make for favorable brain penetration. Figure 9 shows $K_{p,uu}$ data obtained from DLK inhibitors measured in house from various series plotted with E-sol predictions and Table 8 shows some representative examples. We found that to achieve a targeted $K_{p,uu}$ of 0.3, using an E-sol cutoff of -17.1 kcal/mol gives good enrichment with a categorical accuracy of 70%.[26]

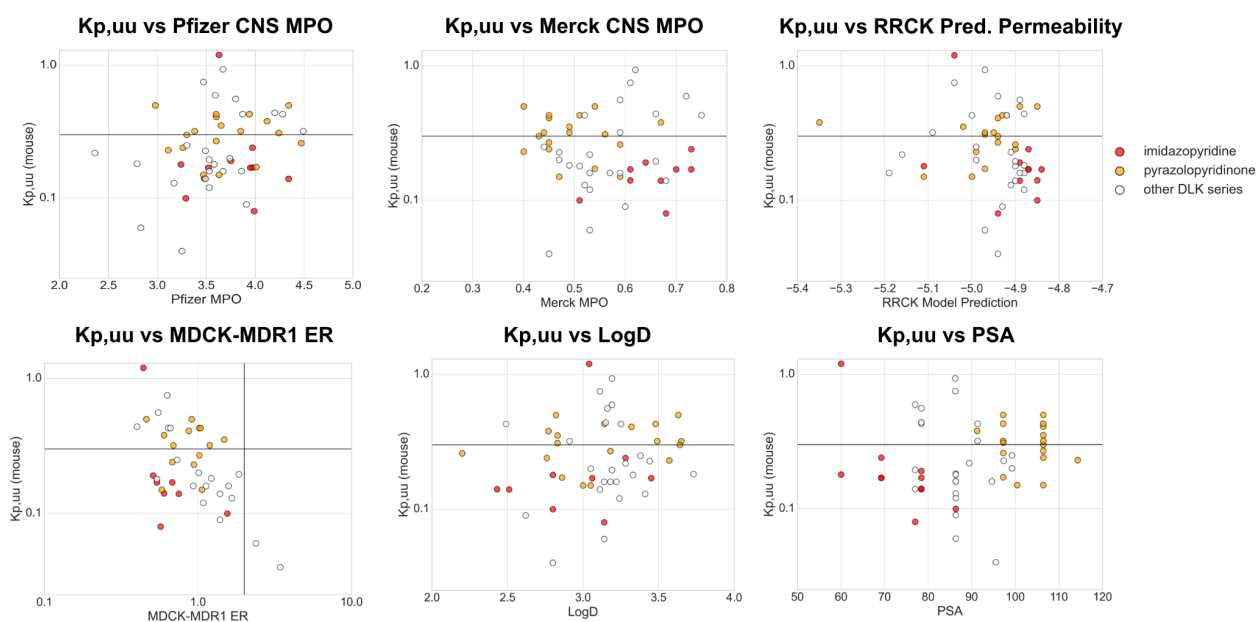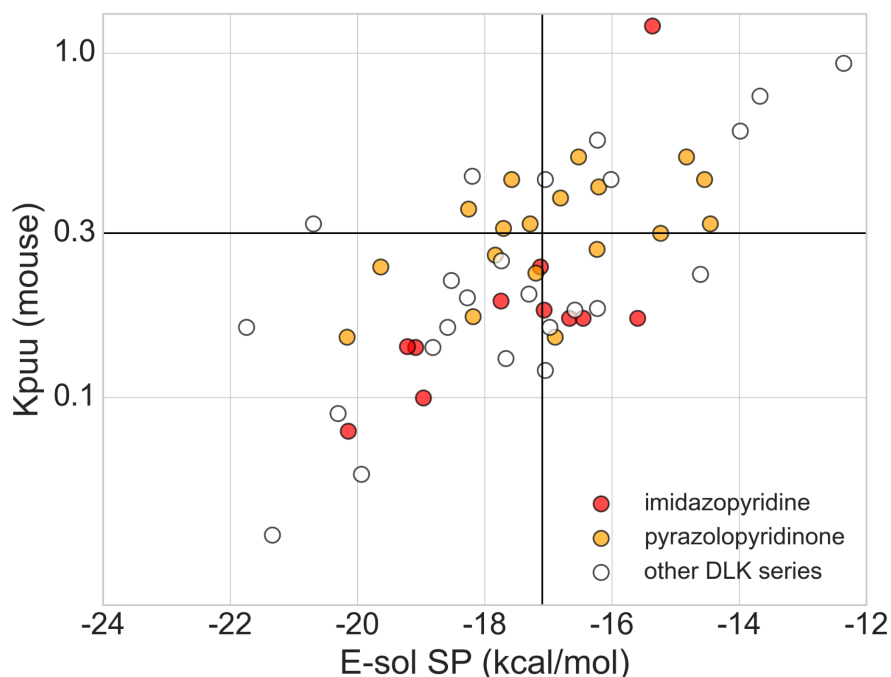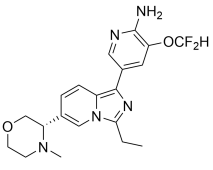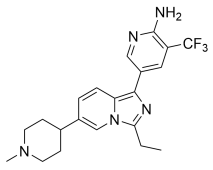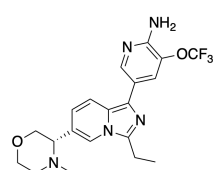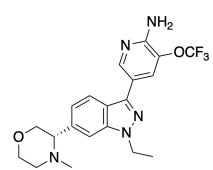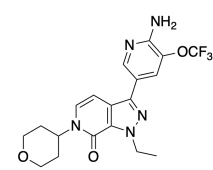**Figure 9**. Correlation of E-sol with $K_{p,uu}$. A total of 53 $K_{p,uu}$ data-points are plotted in log-scale (y-axis) with E-sol (kcal/mol) labeled for individual series (x-axis). We note a target favorable $K_{p,uu}$ of 0.3 with a horizontal line and the E-sol threshold which maximizes categorical accuracy for achieving this target $K_{p,uu}$ with a vertical line (-17.1 kcal/mol). The area under the curve (AUC) from a Receiver Operating Characteristic (ROC) plot of this data is 0.76. We exclude from analysis those compounds with solubility < 1 µM and with brain tissue binding < 2 % as compounds meeting this criteria contribute significant uncertainty to the $K_{p,uu}$ measurements. All brain tissue binding values and other $K_{p,uu}$ metadata are included in SI Table S1.

Table 8. Retrospective correlations between E-sol and $K_{p,uu}$.

Cmpd	Chemical Structure	Merck CNS pMPO	MDCK-MDR1 A→B (10^{-6} cm/s) / ER	PSA	LogD	E-sol (kcal/mol)	$K_{p,uu}$ (mouse)
31		0.67	30.1/0.8	78	2.5	-19.1	0.14
18		0.90	10.6/1.6	59	2.8	-17.1	0.18
26		0.61	37.6/0.7	78	3.3	-17.1	0.24
38		0.59	24.1/0.4	78	3.8	-15.2	0.42
41		0.51	7.6/1.0	97	3.5	-14.6	0.43

Retrospective analysis of imidazopyridine series examples **31**, **18** and **26** shows the disconnect between common CNS predictive properties and their $K_{p,uu}$ readouts. For example, the CNS pMPO score of these three compounds suggested they were likely to be brain penetrant however looking at the experimental readouts, that is not always the case as shown for compounds **31** and **18**. This is as compared to their E-sol predictions, which ranked them much

more accurately. Indazole series example **38** shows a favorable CNS pMPO score and E-sol value, which led to a good $K_{p,uu}$. When shifting efforts to the pyrazolopyridinone series, we began using this method prospectively, beginning lead optimization from a favorable starting point which had both good E-sol and $K_{p,uu}$ (**41**). The prospective application of E-sol is outlined in the next few SAR tables, where we employed a number of models in parallel to improve potency and selectivity whilst balancing the ADME and PK profiles of the pyrazolopyridine series.

Table 9. Initial SAR on pyrazolopyridinone series.
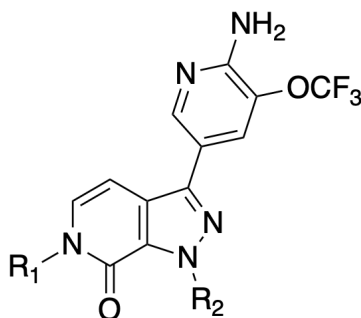
Cmpd	R_1	R_2	FEP Predicted K_i (nM)	DLK K_i (nM)	p-JNK cell IC_{50} (nM)	mLM/hLM (µL/min/mg)	E-sol (kcal/mol)	$K_{p,uu}$ (mouse)
41		Et	4.6	2.8	110	16/8.8	-14.6	0.43
43		cPr	5.4	3.4	104	17/13	-14.6	0.31
44		Et	11.0	10.5	440	24/9.2	-14.8	0.50
45		Et	9.2	7.7	120	33/22	-14.3	na
46		Et	3.5	1.3	140	25/18	-14.4	0.29

Cmpd	R_1	R_2	FEP Predicted K_i (nM)	DLK K_i (nM)	p-JNK cell IC_{50} (nM)	mLM/hLM (μL/min/mg)	E-sol (kcal/mol)	$K_{p,uu}$ (mouse)
47		Et	n/a	2.5	130	4/<3	-16.8	0.38
48		Et	3.1	3.0	130	8.3/7.9	-20.2	0.15
49		Et	1.4	1.5	110	10/<4	-11.7	0.38[a]
50		Et	4.1	1.9	85	24/9.3	-17.6	0.43
51		Et	1.6	1.9	94	8.3/14	-16.2	0.41

[a]*Brain tissue binding < 2%*

Compound **41** with a THP solvent exposed group is potent with DLK K_i of 2.8 nM, with favorable human and mouse microsomal stability, and good brain penetration as indicated by $K_{p,uu}$ of 0.43 in mouse (Table 9). While exploring R_1 and R_2 SAR, FEP and E-sol were both calculated to prioritize potent DLK inhibitor designs with higher probability of brain penetration. R_2 substitution was explored by FEP to engage p-loop interactions, with cPr being similar potency to Et (**43** vs. **41**) and larger substitutions were not tolerated. Different ring sizes (R_1) were explored and in line with FEP predictions, the 7-membered ring (**46**) was the most potent and the smaller, oxetanyl ring (**44**) the least potent. Piperidine analog **47** shows similar potency vs. THP analog **41**, excellent *in vitro* ADME profiles and good brain penetration as predicted by E-sol ($K_{p,uu}$ = 0.38, E-sol = -16.8 kcal/mol). However, this compound shows weak hERG inhibition (IC_{50} 7 μM), as was expected given its predicted pK_a of 8.3. As described earlier, modulating pK_a of piperidine by incorporating an oxetanyl group gives **48** with hERG IC_{50} of >30 μM. Unfortunately, as predicted by the unfavorable E-sol (-20.2 kcal/mol), **48** shows lower brain penetration ($K_{p,uu}$ of

0.15). Testing negative compounds *in vivo* once in a while further validated the impact of utilizing E-sol to guide the design of brain-penetrant molecules. An analog with a smaller R_1 substitution such as **49** is quite potent in DLK biochemical inhibition assay, however, it is highly lipophilic and it has poor aqueous solubility. Substitution on the THP ring was attempted, identifying trans-methoxy and cis-methoxy substituted analogs (**50** and **51**) with improved DLK K_i. Both enantiomers demonstrated favorable *in vitro* ADME profiles, good to excellent oral exposure (%F = 36 for **50** and 71 for **51** in mouse PK) and desirable brain penetration as predicted by E-sol (Table 9).

In terms of kinome selectivity, pyrazolopyridinone analog **41** provided us with a decent starting point as indicated by its S-scores (S(35) = 0.114, S(10)=0.037 and S(1)=0.005) from single concentration (0.5 μM, 100x over DLK K_d) ScanMax screening at Eurofins (Figure 11). Follow up K_d determination of the top hits confirmed the key top off-target kinases, with K_d ratios relative to DLK between 2-50 fold (Table 10). These include LZK (closest DLK homolog), MEK5, PAK4, FLT3, TRKA and KIT. Chronic neurological diseases require a high degree of on-target selectivity and our ultimate goal was >100 fold selectivity against these off-targets. In an effort to achieve that, we established FEP models for each of these kinases using either available X-ray structures or by building homology models. To streamline our prospective off-target FEP profiling workflow and reduce computational cost, we used sequence similarity and correlation of measured potencies (R^2 > 0.85), to select FLT3 as a surrogate for both TRKA and KIT. We then established a 4 off-target FEP MPO score based on prospective profiling of each design idea against LZK, MEK5, FLT3, and PAK4 *in silico*. The predictions were then validated experimentally by testing each synthesized compound through a panel with all 6 off-targets (LZK, MEK5, PAK4, FLT3, TRKA and KIT). Figure 10 below shows the good prospective FEP performance across all four primary off-targets.
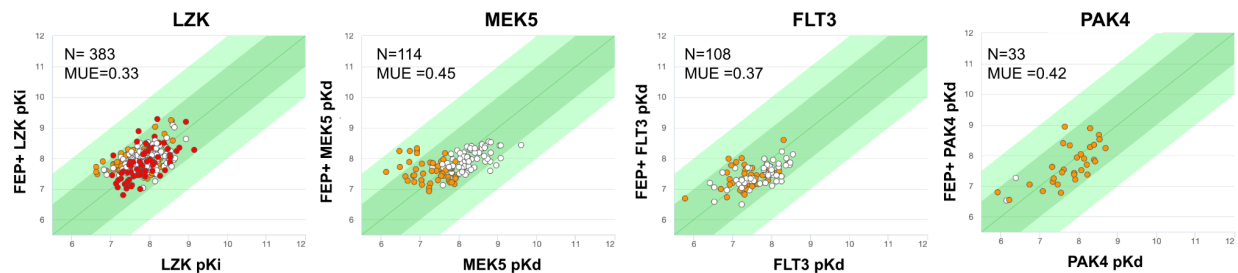
Figure 10. Prospective FEP selectivity performance for four key off target proteins predicted binding affinities compared with measured results. The mean unsigned error (MUE) is reported in pK_d or pK_i units. Series are colored as red for the imidazopyridines, orange for the pyrazolopyridinones and white for other DLK series.

Our FEP selectivity score indicated that addition of a chiral methoxy group to the THP group, in a *cis* (S,S) configuration was going to be beneficial for selectivity. *Cis* analog **51** was made and confirmed to have improved selectivity compared to its parent compound **41** as well as its *trans* isomer **50** as shown in the selectivity scores (Table 10) and ScanMax tree plot (Figure 11). Table 10 compares the selectivity ratios for the plain THP **41**, with the *trans* **50** and *cis* **51** configuration of the methoxy group for each of the off-targets.

Table 10. Top off-target kinase K_d ratio over DLK potency.

Cmpd	LZK/DLK (K_i^a ratio)	FLT3/DLK (K_d ratio)	TRKA/DLK (K_d ratio)	KIT/DLK (K_d ratio)	MEK5/DLK (K_d ratio)	PAK4/DLK (K_d ratio)	FEP off-target Selectivity MPO[b]	Exp off-target Selectivity MPO[c]
41	4.6	12	2.3	4.0	7.2	50	0.20	0.18
50	4.3	10	6.9	4.9	35	65	0.37	0.26
51	12	32	24	22	14	22	0.45	0.49

[a]LZK K_i was determined by in-house assay; [b]FEP predicted MPO for four off-target kinases (LZK, MEK5, FLT3, and PAK4); [c]Experimental MPO for 6 off-target kinases (LZK, MEK5, PAK4, FLT3, TRKA and KIT) .
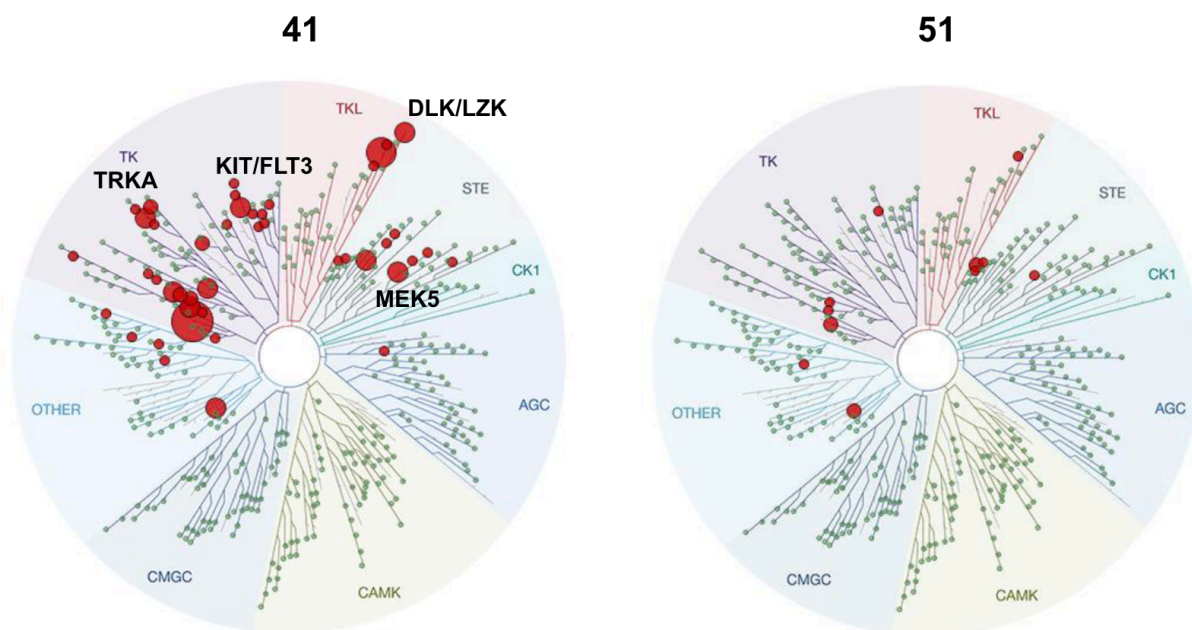
Figure 11. Selectivity Profiles of **41** and **51**. Kinome selectivity was obtained from KINOMEscan™ (Eurofins) using 0.5 µM of **41** (100x over DLK K_d) or 0.1 µM of **51** (100x over DLK K_d) against 468 kinases. Top off-target kinases are labeled on the plot of **41**.
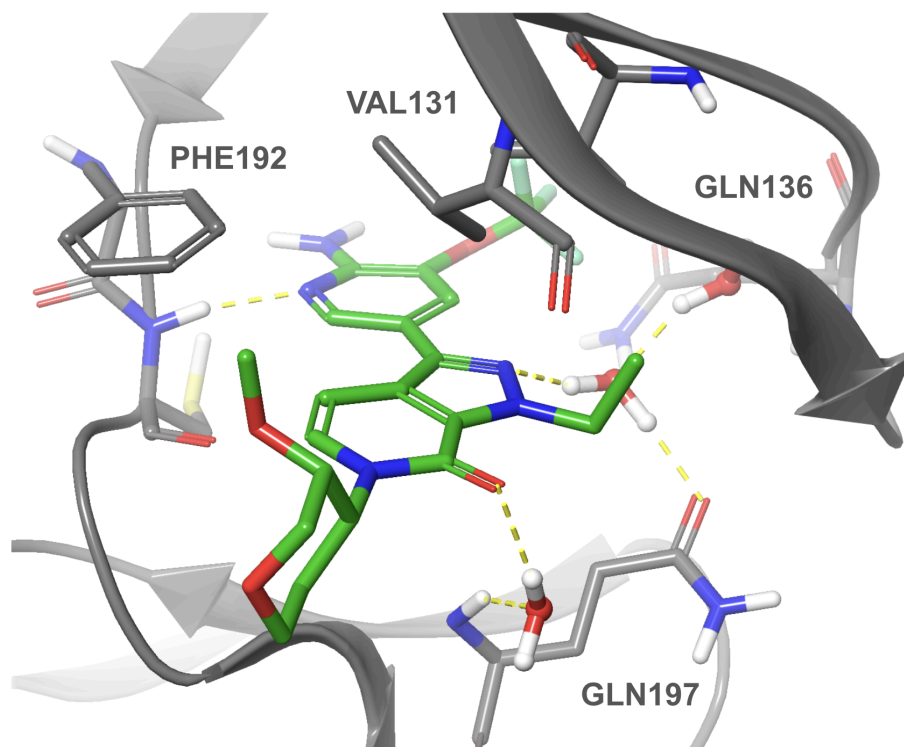
Figure 12. Co-crystal structure of human DLK with **51**. Only key residues are shown for clarity.

Co-crystal structure of **51** (Figure 12) shows the key interactions of the molecule with the DLK amino acid residues in the active site. This structure highlights the water network between the pyrazolopyridinone core and GLN197. The THP chiral methoxy group points up to the P-loop solvent interface of the pocket, towards residue VAL131. Our hypothesis for the improved selectivity for **51** lies in differences in packing near this residue, where VAL131 in DLK is a bulkier leucine or isoleucine residue in the key off-target kinases. The *cis* presentation of the methoxy group would clash with the larger residues in our off-target kinases, reducing off-target potency, whilst maintaining on target potency. Based on this, we designed compounds with the aim to further improve selectivity (Table 11). In line with our hypotheses, the FEP models indicated that addition of even larger groups at the chiral methoxy position would improve selectivity. Indeed, analog **52** with cPr at this position gave a significant boost in measured

selectivity, as did OCF$_3$ **55** and O-cBu **56**. We also explored the impact of the hinge region on selectivity as exemplified with **52**, **53** and **54**. Compared to CF$_3$ analog **54** and OCF$_3$ analog **52**, the OCF$_2$H analog **53** gives better DLK potency and selectivity, although FEP underpredicted selectivity for this hinge change. Overall, using FEP potency predictions, FEP selectivity MPO, and E-sol allowed for enriched decision making in the identification of promising analogs with improved selectivity and good brain penetration.

Table 11. Pyrazolopyridinone series SAR to improve selectivity.
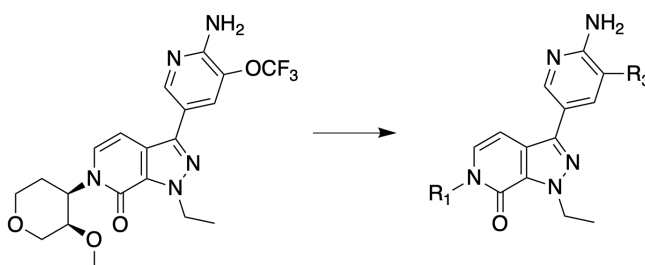
Cmpd	R$_1$	R$_3$	DLK FEP Pred/Exp K$_i$ (nM)	p-JNK cell IC$_{50}$ (nM)	FEP Selectivity MPO[a]	Exp Selectivity MPO[a]	E-sol (kcal/mol)	K$_{p,uu}$ (mouse)
51		OCF$_3$	1.6/1.9	94	0.4	0.5	-16.2	0.41
52		OCF$_3$	0.69/1.3	95	0.6	0.7	-16.3	0.22
53		OCF$_2$H	0.43/0.58	32	0.4	0.8	-16.9	0.15
54		CF$_3$	4.7/1.8	180	na	0.7	-16.9	0.24
55		OCF$_2$H	0.43/0.92	46	0.5	0.7	-16.5	0.50
56		OCF$_2$H	0.26/0.65	35	0.6	0.8	-17.5	na

[a]FEP predicted MPO for four off-target kinases and measured MPO for 6 off-target kinases.

In parallel to the selectivity work, while analog **51** demonstrated a desirable overall profile, it showed high IV clearance in dogs consistent with its high intrinsic clearance in dog liver

microsomes (Table 12). Metabolite identification study in dog liver microsomes suggested that the high clearance is largely driven by oxidation of the THP ring and demethylation of the methoxy group. As shown in Table 12, blocking O-demethylation with O-cPr (**52**) only slightly improved the clearance profile in dogs, while blocking the hotspots on the THP by inserting a spiro-cPr group (**57**) was much more effective. Replacing the THP with a substituted N-methyl piperidine (**58**) reduced the clearance in dog liver microsomes, however, now the introduced N-demethylation pathway became problematic in human and mouse liver microsomes where higher clearance was observed. Dog IV cassette PK was performed and demonstrated that analogs with lower microsomal clearance indeed have reduced dog clearance *in vivo*. Finally, replacing THP with the *cis*-substituted difluorocyclohexyl group, compound **59** was found to be stable across all three species. KAI-11101 (**59**) was also predicted and tested to have picomolar potency (0.7 nM DLK K_i). The high FEP Selectivity MPO score of 0.98 translated to excellent kinome-wide selectivity (S(35) = 0.025, S(10)=0.01 and S(1)=0) due to a combination of the selective OCF_2H hinge and *cis*-methoxy substituents. *In vivo* PK properties of **59** in mouse were also quite favorable with a low clearance (5 ml/min/kg), long half life ($t_{1/2}$ 4.8 h), good bioavailability (%F = 52), and its favorable E-sol value of -17.5 kcal/mol translated to a good $K_{p,uu}$ (0.3 based on AUC). Given the attractive potency, selectivity and PK properties, KAI-11101 (**59**) was selected for further profiling in *ex vivo* DRG assays as well as *in vivo* PD study.

Table 12. Pyrazolopyridinone series SAR to improve dLM CLint.
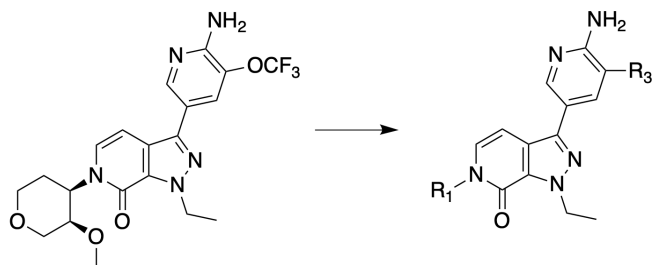
Cmpd	R_1	R_2	R_3	FEP Pred/Exp K_i (nM)	p-JNK cell IC_{50} (nM)	LM CLint m/d/h (µL/min/mg)	FEP/Exp off-target Selectivity MPO[a]	E-sol (kcal/mol)	$K_{p,uu}$ (mouse)
51		Et	OCF_3	1.6/1.9	94	8.3/96/14	0.4/0.5	-16.2	0.41
52		Et	OCF_3	0.69/1.3	95	21/21/12	0.6/0.7	-16.3	0.22
57		Et	OCF_3	1.1/2.2	200	9.7/5.4/3.2	na	-16.1	na
58		Et	OCF_3	1.1/1.1	130	66/21/41	na	-16.5	na
59 KAI-11101		Et	OCF_2H	0.59/0.69	51	18/5.8/<3	1.0/0.9	-17.5	0.30

[a]FEP predicted MPO for four off-target kinases and measured MPO for 6 off-target kinases.

Table 13. Predicted, biochemical and cellular potencies for compound **59** compared to clinical compound GDC-0134.

Assay	GDC-0134 (GNE Ph1)	KAI-11101 (**59**)
FEP Predicted DLK K_i (nM)	n/a	0.6
DLK/LZK K_i (nM)	3.5/7.0	0.7/15
pJNK DLK IC_{50} (nM)	79	51
DRG p-cJun[a], IC_{50} (nM)	301	95
DRG axon protection[a], EC_{50} (nM)	475	363
DRG axon protection[a], max protection (% of DMSO)	75	72

[a]Paclitaxel axonal injury model.

Table 13 summarizes the measured potencies of KAI-11101 (**59**) which potently inhibits DLK activity with 0.7 nM K_i and 51 nM cellular pJNK IC_{50}. In the *ex vivo* DRG CIPN assay, KAI-11101 shows inhibition of paclitaxel-induced MAPK pathway activation through reduction of phosphorylated cJun (p-cJun; IC_{50} = 95 nM) (Figure 13, A) and also demonstrated phenotypic protection against paclitaxel-induced axon degeneration (EC_{50} = 363 nM). More potent inhibition, as well as stronger neuroprotective effects, are observed with KAI-11101 compared to Genentech's Phase 1 candidate GDC-0134 (Figure 13, A and B).
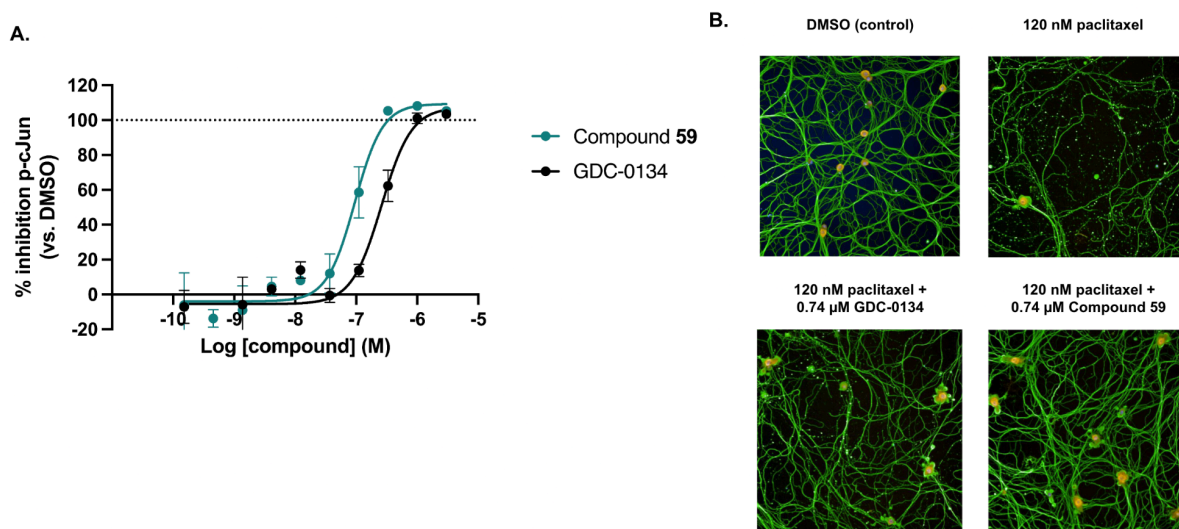
Figure 13. **A**. DLK inhibitors inhibit phosphorylated cJun (p-cJun) induction following paclitaxel treatment in DRG neurons. phospho-cJun staining was quantified by automated script-based image analysis and nuclear intensity was quantified relative to untreated controls. Data are mean and SEM of three technical replicates. **B**. Representative high content images of cultured primary mouse dorsal root ganglion neurons including untreated control neurons and paclitaxel treated neurons in the presence or absence of 0.74 µM KAI-11101 or GDC-0134 (images taken 72 hours after paclitaxel treatment).

In vivo, KAI-11101 demonstrated linear increase in brain exposure and dose-dependent target engagement as measured by inhibition of p-cJun in mouse cerebellum where DLK is constitutively active (Figure 14).[27] Based on the relationship between the reduction in p-cJun

and total brain concentration, cerebellum p-cJun *in vivo* IC$_{50}$ was calculated as 31 nM (1003 ng/g total, 14.5 ng/g unbound based on F$_{u,b}$ = 0.0145), which correlates well with *in vitro* HEK293 pJNK IC$_{50}$ of 51 nM.
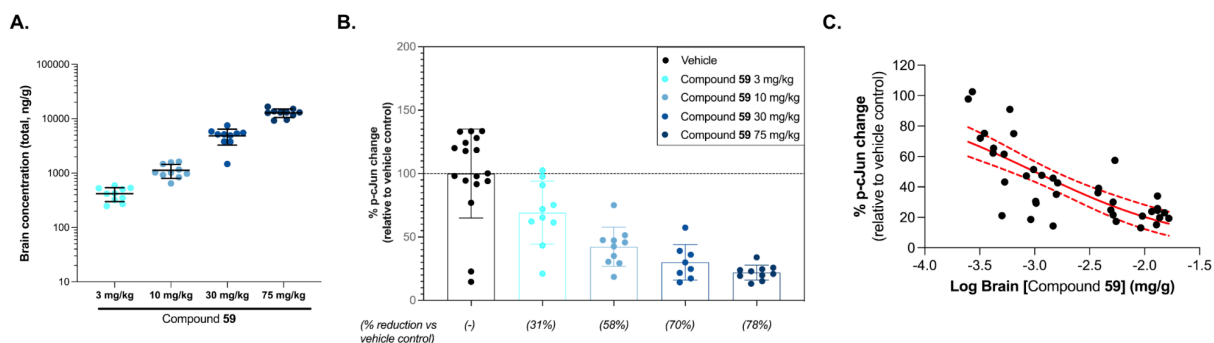
Figure 14. **A**. Dose-dependent KAI-11101 total brain concentration 2 hours post-administration (PO). Data are mean with standard deviation of 10 samples per group. **B**. Dose-dependent reduction in cerebellum phosphorylated cJun (p-cJun) 2 hours post-administration of KAI-11101. p-cJun levels were quantified by Jess Western and normalized to total protein levels in each sample. Data are mean with standard deviation of 17 (vehicle) and 8-10 (treated) samples per group. **C**. Relationship between percentage p-cJun reduction and total brain levels of KAI-11101.

KAI-11101 demonstrated desirable oral PK profiles across four preclinical species and good brain penetration in rodents (Table 14). The *in vivo* clearance in dogs was found to be greatly under-predicted by both liver microsomal and hepatocyte stability data (~10x) which suggested extrahepatic clearance mechanism(s). Dog specific *N*-methylation has been previously reported[28] and *N*-methylated metabolites of KAI-11101 have been detected in incubations with dog hepatocytes *in vitro* and in plasma of dogs dosed orally with KAI-11101. However, a bile duct-cannulation (BDC) study in dogs may be needed to further elucidate the contribution of this pathway in the clearance of KAI-11101 in this species. In contrast, *N*-methylation of KAI-11101 was not observed with rat, monkey, and human hepatocytes. KAI-11101 has good *in vitro* safety profiles (hERG IC$_{50}$ = 9 µM and hepG2 cytotoxicity IC$_{50}$ = 52 µM). It was tested negative in both

Ames and *in vitro* micronucleus assays. In Eurofins ScanMax kinase selectivity panel, it demonstrated >100x selectivity relative to tested kinases, with the exception of LZK and PAK4 (DLK K_i ratios equal to 24 and 10, respectively using functional LZK and PAK4 inhibition assays). KAI-11101 shows no hits in Eurofins *in vitro* Safety-87 pharmacology profiling panel at 10 µM. Preliminary predicted human dose of KAI-11101 ranges from 80 mg to 250 mg QD dosing to cover pJNK IC_{50} at trough (C_{trough} coverage over dosing period was shown to be necessary to achieve neuro protection in both a mouse CIPN[7] and an optic nerve crush efficacy model[4]). Although KAI-11101 has some minor CYP3A TDI (27.5% Δ CYP3A inhibition at 30 µM), further evaluation of its CYP3A TDI kinetic parameters (K_i 170 µM, k_{inact} 0.07 min^{-1}) and $C_{max,u}$ (0.05-0.17 µM) at predicted human efficacious dose suggested its clinical DDI risk would be low. Based on its overall favorable profiles, KAI-11101 was selected as a preclinical candidate for further tox evaluation.

Table 14. KAI-11101 preclinical PK profile.[a]

	CL (ml/min/kg)	V_{ss} (L/kg)	$t_{1/2}$ (h)	F (%)	Brain $K_{p,uu}$ (AUC)
Mouse	5.3	1.6	4.8	53	0.3-0.5[b]
Rat	8.3	4.3	7.2	57	0.6
Dog	24	8.8	6.6	81	-
Cyno	5.5	4.8	12	52	-

[a]IV formulation: DMSO/Solutol HS15/Saline (5/5/90); PO: 0.5%MC (4000 cP) in water; [b]$K_{p,uu}$ range obtained from CD1 mice with PO dosing at 5 mpk, 25 mpk and 75 mpk based on AUC.

DISCUSSIONS AND CONCLUSIONS

Leveraging FEP technology and predictive ADMET modeling tools, we have successfully discovered and optimized a potent, selective and brain-penetrant DLK inhibitor. Starting our discovery campaign from a minimal hinge binding fragment, we took a FEP-guided stepwise approach which enabled the rapid identification of several highly ligand efficient hit series. From these efforts we progressed the imidazopyridine series. During the hit to lead development stage, by reducing the hERG liability via a pK_a-predictive workflow, compound **26** was identified as an early lead molecule with overall desired profiles. Unfortunately, **26** and its close analogs displayed a strong CYP3A TDI signal which could not be easily resolved. Again, guided by the predictive power of FEP, we were able to rapidly identify alternative, potent core systems, such as the pyrazolopyridinones, that were void of the TDI liability. Advancing this series further, we improved brain penetration using a novel QM-based energy of solvation method (E-sol) for the prediction of $K_{p,uu}$ and optimized the selectivity profile through an off-target FEP workflow. This led to the discovery of KAI-11101 (**59**), which has excellent *in vitro* DLK potency and kinase selectivity. It also demonstrated favorable preclinical PK, including good CNS penetration, and *in vitro* safety profiles. In mouse DRG *ex vivo* CIPN assay, KAI-11101 demonstrated strong target engagement as well as phenotypic protection of axon degeneration. In an *in vivo* mouse cerebellum PD model, with linear increase of brain exposure, KAI-11101 demonstrated dose-dependent reduction of p-cJun. KAI-11101 was selected as a promising preclinical candidate.

Throughout the course of this program, we were able to tackle a number of common medicinal chemistry challenges by integrating *in silico* workflows. For predicting binding affinity, the overall FEP performance was excellent on the DLK project, allowing accurate profiling of 27,348 ideas across multiple series with a mean unassigned error of 0.4 pIC_{50} against DLK experimental data.

Accurate FEP predictions allowed our synthetic efforts to be focused on the compounds that would be potent, and as a result, we only had to synthesize ~1000 compounds before identifying our preclinical candidate. Not only did FEP calculations play a key role in driving the program's progression, we established and applied various other physics-based methods to help tackle multiple challenges including hERG inhibition, CYP3A time-dependent inhibition, and off-target kinases selectivity. On tackling brain penetration, we believe the strong correlation shown between E-sol and $K_{p,uu}$ will be impactful to the wider field of CNS drug discovery. Taken together, all of these predictive models allowed us to efficiently discover a promising preclinical candidate with neuroprotective properties.

EXPERIMENTAL SECTION

Scheme 1. Synthesis of KAI-11101 (Compound 59)[a]
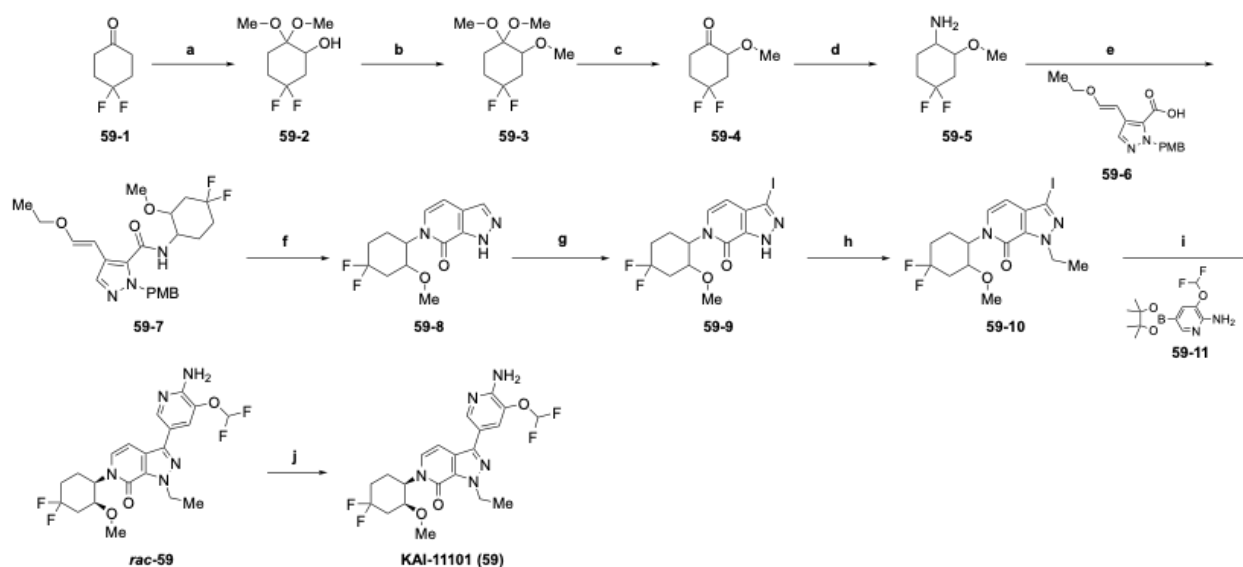
[a]Reagents and conditions: (a) KOH, I₂, MeOH, rt, 81%; (b) MeI, NaH, THF, rt, 75%; (c) 4M HCl, THF, water, rt, 4 h, 88%; (d) ammonium acetate, NaBH₃CN, 50 °C, 2 h; (e) **59-6**, HATU, DIPEA, DMF, rt, 46%; (f) TFA, toluene, 80 °C, 79%; (g) I₂, Cs₂CO₃, DMF, rt; (h) EtI, NaH, DMF, rt, 49%; (i) **59-11**, Pd(dppf)Cl₂, K₂CO₃ , X-Phos, 1,4-dioxane, water, 110 °C, 36%; (j) chiral SFC.

Synthesis of KAI-11101 (**59**) started from 4,4-difluorocyclohexanone **(59-1)**, which was converted to 4,4-difluoro-2-methoxy-cyclohexanamine **(59-5)** in 4 steps through hydroxylation, methylation and reductive amination. Cyclohexanamine was reacted with 4-[(*E*)-2-ethoxyvinyl]-2-[(4-methoxy phenyl)methyl]pyrazole-3-carboxylic acid to form the amide **(59-7)**, which was cyclized under acidic conditions to give the pyrazolopyridinone core **(59-8)**. The pyrazole ring was then decorated by iodination at 3-position **(59-9)** and ethylation at 1-position **(59-10)**. The iodide was further engaged in Suzuki coupling to yield a racemic *cis-* and *trans-* KAI-11101 **(rac-59)**. Final chiral separation gave enantiomerically pure KAI-11101 **(59)**.

Synthesis of 3-(6-Amino-5-(difluoromethoxy)pyridin-3-yl)-6-((1R,2S)-4,4-difluoro-2-methoxy cyclohexyl)-1-ethyl-1,6-dihydro-7H-pyrazolo[3,4-c]pyridin-7-one KAI-11101 (59).

Step A: *5,5-Difluoro-2,2-dimethoxycyclohexan-1-ol (59-2)*. To a solution of **59-1** (4.7 g, 35.0 mmol), KOH (11.8 g, 210 mmol) in MeOH (350 mL) was added iodine (9.9 g, 77.1 mmol) at 0 °C over a period of 180 min under a N_2 atmosphere. Then the reaction mixture was allowed to warm to rt and stirred for 3 h. The reaction mixture was concentrated, dissolved in ethyl acetate (300 mL), and filtered to remove inorganic salts. The filtrate was concentrated and purified by flash column chromatography (0–30% EtOAc in petroleum ether) to give the title compound (5.6 g, 81% yield) as a yellow oil. ^{1}H NMR (400 MHz, DMSO-d_6) δ 4.92 (d, *J* = 4.4 Hz, 1H), 3.81 (d, *J* = 1.7 Hz, 1H), 3.18 – 3.12 (m, 6H), 2.05 (dd, *J* = 9.5, 4.1 Hz, 1H), 2.02 – 1.82 (m, 3H), 1.81 – 1.61 (m, 2H).

Step B: *4,4-Difluoro-1,1,2-trimethoxycyclohexane (59-3)*. To a suspension of NaH (2.3 g, 57.1 mmol, 60% purity) in THF (250 mL) at 0 °C was added a solution of **59-2** (5.6 g, 28.5 mmol) in

THF (100 mL). The mixture was stirred at 0 °C for 30 min and methyl iodide (5.31 mL, 85.6 mmol) was added dropwise. After stirring at rt for 2 h, the reaction mixture was poured into water with ice and extracted with EtOAc (200 mL × 3). The organic layer was dried over anhydrous sodium sulfate, filtered, and concentrated to give a residue which was purified by flash column chromatography (0–20%, EtOAc in petroleum ether) to give the title compound (4.5 g, 75% yield) as colorless oil. ^{1}H NMR (400 MHz, DMSO-d_6) δ 3.51 (q, J = 3.5 Hz, 1H), 3.29 (s, 3H), 3.14 (s, 3H), 3.12 (s, 3H), 2.39 – 2.27 (m, 1H), 2.05 – 1.78 (m, 3H), 1.77 – 1.72 (m, 2H).

Step C: *4,4-Difluoro-2-methoxycyclohexan-1-one (**59-4**)*: To a solution of **59-3** (4.5 g, 21.4 mmol) in THF (200 mL) was added 4 M HCl (30 mL) at 0 °C. The reaction mixture was allowed to warm to rt and stirred for 4 h. The reaction mixture was concentrated, diluted with EtOAc (50 mL), and concentrated again. The crude mixture was diluted with EtOAc (150 mL), neutralized with NaHCO$_3$ aqueous solution at 0 °C, and extracted with EtOAc. The organic layer was dried over anhydrous sodium sulfate, filtered, and concentrated to give a residue which was purified by flash column chromatography (0–25%, EtOAc in petroleum ether) to give the title compound (3.1 g, 88% yield) as a yellow oil. ^{1}H NMR (400 MHz, CDCl$_3$) δ 3.96 (dd, J = 11.9, 6.5 Hz, 1H), 3.48 (s, 3H), 2.83 – 2.70 (m, 1H), 2.64 – 2.51 (m, 2H), 2.48 – 2.37 (m, 1H), 2.25 – 2.13 (m, 2H).

Step D: *4,4-Difluoro-2-methoxycyclohexan-1-amine (**59-5**)*: To a solution of **59-4** (2.4 g, 14.6 mmol) in MeOH (150 mL) was added ammonium acetate (4.5 g, 58.5 mmol) and NaBH$_3$CN (3.2 g, 51.2 mmol). The reaction was stirred at 50 °C for 2 h. The mixture was concentrated and the residue was diluted with DCM (200 mL). The mixture was further stirred at rt for 0.5 h. The mixture was filtered and concentrated to give the title compound (1.1 g, crude) as a yellow oil. MS (ESI$^+$): *m/z* 166.1 [M + H]$^+$.

Step E: *(E)-N-(4,4-Difluoro-2-methoxycyclohexyl)-4-(2-ethoxyvinyl)-1-(4-methoxybenzyl)-1H-pyrazole-5-carboxamide (**59-7**)*: A solution of **59-5** (800 mg, 4.84 mmol), **59-6** (1.5 g, 4.84 mmol), DIPEA (1.9 g, 14.53 mmol) and HATU (2.8 g, 7.26 mmol) in DMF (60 mL) was stirred at

rt for 1 h under N_2 atmosphere. The reaction mixture was poured into water with ice and extracted with EtOAc (300 mL × 3). The organic layer was dried over anhydrous sodium sulfate, filtered, and concentrated to give a residue which was purified by flash column chromatography (0–25%, EtOAc in petroleum ether) to give the title compound (1.0 g, 46% yield) as a colorless oil. MS (ESI⁺): *m/z* 450.5 [M + H]⁺.

Step F: *6-(4,4-Difluoro-2-methoxycyclohexyl)-1,6-dihydro-7H-pyrazolo[3,4-c]pyridin-7-one (59-8):* To a solution of **59-7** (1.0 g, 2.22 mmol) in toluene (10 mL) was added TFA (10 mL). The mixture was sealed and stirred at 80 °C for 1.5 h. The reaction was concentrated, diluted with DCM (200 mL), neutralized with $NaHCO_3$ aqueous solution at 0 °C, and extracted with DCM (200 mL × 3). The organic layer was dried over anhydrous sodium sulfate, filtered, and concentrated to give a residue which was purified by flash column chromatography (0–5%, MeOH in DCM) to give the title compound (500 mg, 79% yield) as a yellow oil. MS (ESI⁺): *m/z* 284.3 [M + H]⁺.

Step G: *6-(4,4-Difluoro-2-methoxycyclohexyl)-3-iodo-1,6-dihydro-7H-pyrazolo[3,4-c]pyridin-7-one (59-9):* To a solution of **59-8** (500 mg, 1.77 mmol) in DMF (20 mL) was added Cs_2CO_3 (1.7 g, 5.30 mmol) and I_2 (896 mg, 3.53 mmol). The mixture was stirred at rt for 2 h. The reaction mixture was concentrated to give the title compound (260 mg, crude) as a yellow oil, which was used for the next step without further purification. MS (ESI⁺): *m/z* 410.3 [M + H]⁺.

Step H: *6-(4,4-Difluoro-2-methoxycyclohexyl)-1-ethyl-3-iodo-1,6-dihydro-7H-pyrazolo[3,4-c] pyridin-7-one (59-10):* To a solution of **59-9** (500 mg, 1.22 mmol) in DMF (30 mL) was added NaH (196 mg, 4.89 mmol, 60% purity) and ethyl iodide (229 mg, 1.47 mmol). The mixture was stirred at rt for 2 h. The mixture was concentrated and purified by flash column chromatography (EtOAc:petroleum ether = 5:1) to give the title compound (260 mg, 49% yield) as a white solid. MS (ESI⁺): *m/z* 438.4 [M + H]⁺.

Step I: *3-(6-Amino-5-(difluoromethoxy)pyridin-3-yl)-6-((1RS,2SR)-4,4-difluoro-2-methoxy cyclohexyl)-1-ethyl-1,6-dihydro-7H-pyrazolo[3,4-c]pyridin-7-one* (**rac-59**): A solution of **59-10** (260 mg, 0.60 mmol), **59-11** (171 mg, 0.60 mmol), X-phos (56.74 mg, 0.12 mmol), Pd(dppf)Cl$_2$ (87.26 mg, 0.12 mmol) and K$_2$CO$_3$ (247 mg, 1.79 mmol) in 1,4-dioxane (12 mL) and H$_2$O (3 mL) was stirred at 95 °C for 2 h. The reaction was concentrated and purified by flash column chromatography (DCM:MeOH = 10:1) to give a crude product (180 mg). The crude product was further purified by prep-HPLC (ACN/water/0.1% NH$_4$OH) to afford the title compound (100 mg, 36% yield). MS (ESI$^+$): *m/z* 470.6 [M + H]$^+$.

Step J: *3-(6-Amino-5-(difluoromethoxy)pyridin-3-yl)-6-((1R,2S)-4,4-difluoro-2-methoxy cyclohexyl)-1-ethyl-1,6-dihydro-7H-pyrazolo[3,4-c]pyridin-7-one* *(59)*. **Rac-59** (100 mg, 0.21 mmol) was purified by chiral SFC (Daicel IG-3 (4.6 x 100 mm, 3 μm), 35% MeOH [0.2% NH$_3$(7M in MeOH)] in CO$_2$, 100 mL/min, 30 °C) to afford the title compound (34.2 mg, 34% yield) as a white solid (second peak, RT: 1.534 min). ^{1}H NMR (400 MHz, DMSO-d_6): δ 8.30 (d, *J* = 1.9 Hz, 1H), 7.69 (s, 1H), 7.29 – 7.28 (d, 1H), 7.25(s, 1H), 6.79 (d, *J* = 7.5 Hz, 1H), 6.37 (s, 2H), 5.12 (d, *J* = 12.9 Hz, 1H), 4.75 (dt, *J* = 13.6, 6.7 Hz, 2H), 3.74 (s, 1H), 3.14 (s, 3H), 2.68 – 2.55 (m, 1H), 2.42 (dd, *J* = 12.0, 5.8 Hz, 1H), 2.28 – 2.07 (m, 3H), 1.72 (d, *J* = 11.8 Hz, 1H), 1.42 (t, *J* = 7.1 Hz, 3H). MS (ESI$^+$): *m/z* m/z 470.5 [M + H]$^+$. The absolute configuration of **59** was confirmed by comparing with a genuine sample obtained from the process route where the chiral amine of defined configuration was used.

DLK and LZK biochemical assay. Compound inhibition of DLK or LZK activity was measured using an *in vitro* kinase assay using purified His-MKK4 substrate (res. 80-399; K131M, purified inhouse) and recombinant GST-DLK (Carna Biosciences; res. 1-520) or GST-LZK (Carna Biosciences; res. 1-966). The final assay was performed at 10 μL with 50 nM His-MKK4 substrate and 10 nM DLK or 5 nM LZK enzyme in a buffer of 50 mM HEPES pH 7.5, 1 mM

EGTA, 10 mM $MgCl_2$, 2 mM DTT, 0.01% Tween 20, 0.01% Bovine r-Globulin in a white 384 square well OptiPlate (PerkinElmer). Compounds were serially diluted in 100% DMSO from 300 µM and were incubated with DLK or LZK at a final concentration of 0.1% DMSO for 60 minutes before addition of substrate and ATP (final concentration for DLK assay: 100 µM (Tables 1-2) or 500 µM (Tables 3, 4, 6, 7, 9-12); LZK assay: 100 µM in 10 µL kinase reaction). Plates were briefly mixed on a shaker and incubated at room temperature for 30 minutes before addition of anti-phospho-MKK4-Tb (R&D Systems, labeled with terbium by Cisbio; final concentration 0.18 nM in 20 µL detection reaction) and 50 nM anti-His-D2 (Cisbio; final concentration 12.5 nM in 20 µL detection reaction) diluted in HTRF detection buffer (Cisbio). Plates were incubated for 20 hours at 4℃ before the HTRF signal was measured using Envision at emission 665 nm and 615 nm. HTRF signal was converted to percentage of enzyme activity relative to treated with DMSO (0% inhibition) and samples without DLK or LZK enzyme (100% inhibition) and IC50 and Hill coefficients were obtained using Graph Pad Prism (Graph Pad software, Inc, USA) with non-linear regression analysis.

Phospho-JNK Cellular Assay. Compound inhibition of DLK-mediated phosphorylation of the substrate JNK was assessed in HEK293 cells. Briefly, Jump-In T-Rex HEK293 (ThermoFisher) were stably transfected with the human DLK gene (NM_001193511.1) and cultured in DMEM high glucose medium (ThermoFisher) supplemented with 10% dialyzed FBS (ThermoFisher), 40 µg/mL G418 (ThermoFisher) and 5 µg/mL Blasticidin S (ThermoFisher). Fifty microliters of cells were plated in a 96-well tissue culture treated plate (Grenier) in DMEM with 10% dialyzed FBS and 1 µg/mL doxycycline (Sigma) and incubated for 24 hours at 37℃ in a humidified atmosphere of 5% CO2. Compounds were serially diluted in 100% DMSO from 600 µM then transferred to serum free DMEM medium to make diluted compound solutions starting from 6 µM. The final DMSO concentration is 0.5% in 100 µL cell solution. Cells were treated with 50 µL

of diluted compound solutions and incubated for 5 hours at 37℃ in a humidified atmosphere of 5% CO2. Cell supernatant was removed and 50 µL ice cold 1x lysis buffer (Cisbio) was added prior to incubation for 40 minutes at room temperature with shaking. Cell lysate was mixed 4:1 in a 384 well low volume white reaction plate (PerkinElmer) with antibody solution containing 1:1 anti-phospho-JNK-d2 (Cisbio) and anti-phospho-JNK (Cisbio) in detection buffer (Cisbio) and incubated overnight at room temperature before the fluorescence signal was measured using Envision at emission 665 nm and 620 nm. HTRF signal was converted to percentage of JNK phosphorylation using the following equation relative to DMSO (0% inhibition) and 10 µM GNE-3511 (100% inhibition). IC50 and Hill coefficients were obtained using Graph Pad Prism (Graph Pad software, Inc, USA) with non-linear regression analysis.

Phospho-cJun and Axon Degeneration in Paclitaxel Treated Primary Mouse Dorsal Root Ganglion Neurons. Primary dorsal root ganglion (DRG) were isolated from E12.5-13.5 mice (C57/Bl6) and incubated with 0.05% Trypsin solution containing EDTA at 37°C for 30 min. After 1 min gentle centrifugation the trypsin solution was removed and replaced with Neurobasal medium (ThermoFisher) containing 10% fetal bovine serum (ThermoFisher) and 1x penicillin and streptomycin (ThermoFisher). Then, DRG were triturated by gentle pipetting, cell suspensions were washed 2 times with DRG growth medium (Neurobasal medium) containing 2 mM L-glutamine (ThermoFisher), 0.3% glucose (Sigma), 2% B27 (ThermoFisher), 50 ng/mL NGF (Sigma), 10 µM uridine (Sigma), 10 µM 5-fluoro-2′- deoxyuridine (Sigma), 50 U/mL penicillin and streptomycin. DRG neurons were counted with Luna cell counter and further cultured in a 384-well culture dish (Greiner, coated with 100 µg/ml poly-D-lysine hydrobromide [Sigma Aldrich] and 3 µg/ml Laminin mouse protein [Thermo Fisher]) at ~1000 cells/well for 5 DiV in Neurobasal medium (Thermo Fisher) plus B27 supplement (Thermo Fisher). Compounds were serially diluted in culture medium with a final DMSO concentration of 0.2%. Cells were

treated with 10 µL compounds before axon injury was induced by addition of 120 nM paclitaxel (Sigma Aldrich), cells were fixed with paraformaldehyde (Electron Microscopy Sciences) and stained after 20 or 72 hours for phospho-cJun induction or axon degeneration, respectively.

Phospho-cJun was detected by immunofluorescence staining cells for phospho-cJun (Abcam), BIII-tubulin (R&D Systems), NeuN (Millipore), and DAPI (Sigma) and imaging with Opera Phenix. An automated script based image analysis using in house Acapella based scripts (Evotec) was used to analyze phospho-cJun nuclear intensity. Data were normalized to phospho-cJun nuclear intensity for untreated neurons and for paclitaxel with DMSO control treated neurons. IC50 values and Hill coefficients were obtained using Graph Pad Prism (Graph Pad software, Inc, USA) with non-linear regression analysis.

Axon degeneration was detected by immunofluorescence staining cells for BIII-tubulin (R&D Systems), NeuN (Millipore), and DAPI (Sigma) and imaged with Opera Phenix. An automated script based image analysis using in house Acapella based scripts (Evotec) was used to analyze the ridge-to-spot ratio to assess axon fragmentation. Data were normalized to ridge-to-spot ratio for untreated neurons and for paclitaxel with DMSO control treated neurons. EC50 values and Hill coefficients were obtained using Graph Pad Prism (Graph Pad software, Inc, USA) with non-linear regression analysis.

Animal studies. *In vivo* PK studies were performed in accordance with the Chinese Commission on Life Sciences, National Research Council standards, and standard operating procedures (SOPs) of Pharmaron, Inc. *In vivo* PK/PD studies were performed at Evotec in accordance with the regulations of the German animal welfare act and the directive 2010/63/EU of the European Parliament on the protection of animals used for scientific purposes. Protocols were approved by the local ethics committee of the Authority for Health and Consumer Protection of the city and state Hamburg ("Behörde für Gesundheit und Verbraucherschutz"

BGV, Hamburg). Mice were housed on a 12 hour light/dark cycle with *ad libitum* access to food and water. Pharmacokinetic studies to determine plasma and brain exposures were performed in male CD-1 mice following intravenous or oral administration under a fasting condition. For intravenous administration, compounds were dosed using 5% DMSO/10% Solutol HS15/85% saline, and for oral administration compounds were dosed using 0.5% methylcellulose. Mice were euthanized by CO_2 asphyxiation where appropriate while blood samples were drawn via heart puncture for brain exposure studies or via tail vein blood draw for nonterminal samples with K_2EDTA as the anticoagulant. The plasma fractions were separated via centrifugation. Brain samples were homogenized in a ratio of 1:3 with PBS. Both sample types were prepared for LC/MS/MS analysis via protein precipitation. In the PK/PD study, male C57Bl/6J mice 3-4 months of age received a single oral dose of KAI-11101 in a suspension of 0.5% methylcellulose in water at 3, 10, 30 or 75 mg/kg. Terminal tissue collection was conducted 2 hours after treatment (10 mice / group). Mice were euthanized by CO_2 asphyxiation and blood was collected by cardiac puncture into vials containing K_2-EDTA anticoagulant. Then, brains were extracted and the cerebellum was dissected for p-cJun level analysis. The cerebellum was cut into two equal parts then snap frozen in liquid nitrogen and stored at -80°C. Phospho-cJun levels were analyzed from fresh lysate of left cerebellum samples by Jess Western using 2 μg/μL protein per sample with Ser73 p-cJun monoclonal antibody (CST), at a dilution of 1:25. Tissue samples were analyzed across three separate Jess runs, with vehicle samples divided across each run. Total protein levels for each lane were quantified using Jess Western chemiluminescent total protein assay module. p-cJun levels normalized to total protein levels were combined for all groups and percent reduction compared to vehicle control groups was analyzed relative to total brain exposure. Brain tissue samples were homogenized and analyzed for compound bioanalysis as above.

Kinase K_d evaluation for DLK, FLT3, MEK5, PAK4, TRKA, and KIT proteins. Affinity values for DLK, FLT3, MEK5, PAK4, TRKA and KIT were measured by K_dELECT competitive binding assays at DiscoverX (Eurofins).

Computational Models. E-sol QM calculations were performed using Jaguar[29] following the published protocol([26]). Predictions of pK_a values were carried out by either the micro-pK_a or the macro-pK_a[16] protocols using Jaguar.[29] FEP calculations were performed using FEP+[30] and the OPLS4 force field.[14] On-target DLK FEP models were based on PDB 5VO2. Off-target FEP models used PDB 6IL3 for FLT3, PDB 4YNE for TRKA, PDB 5XVA for PAK4. Homology models were constructed using Prime[31] for LZK based on DLK PDB 5VO2, and for MEK5 using PDB 3EQI. Pfizer CNS desirability MPO[22] was implemented in LiveDesign.[32] HBD, MW, PSA, and logP were calculated by RDKit,[33] and Epik pK_a[34] was used to convert from logP to logD at pH 7.4. Merck CNS pMPO[15] was implemented in LiveDesign[32] using a published protocol.[35]

AUTHOR INFORMATION

Corresponding Authors

H. Rachel Lagiakos - Schrödinger Inc., New York, New York, 10036, United States; Email: rachel.lagiakos@schrodinger.com
Zhe Nie - Schrödinger Inc., San Diego, California, 92122, United States; Email: zhe.nie@schrodinger.com; orcid.org/0009-0009-5125-8929

Authors
Yefen Zou - Schrödinger Inc., San Diego, California, 92122, United States

Hideyuki Igawa - Schrödinger Inc., New York, New York, 10036, United States; orcid.org/0009-0007-3802-6344

Eric Therrien - Schrödinger Inc., New York, New York, 10036, United States; orcid.org/0000-0003-3306-9162

Morgan Lawrenz - Schrödinger Inc., San Diego, California, 92122, United States; orcid.org/0000-0002-4798-6423

Mats Svensson - Schrödinger Inc., New York, New York, 10036, United States

Mitsunori Kato - Schrödinger Inc., New York, New York, 10036, United States; orcid.org/0000-0002-8426-2504

Felicia Gray - Schrödinger Inc., Portland, Oregon, 97204, United States

Kristian K. Jensen - Schrödinger Inc., New York, New York, 10036, United States

Markus K. Dahlgren - Schrödinger Inc., New York, New York, 10036, United States

Robert D. Pelletier - Schrödinger Inc., New York, New York, 10036, United States; orcid.org/0000-0003-2112-1461

Karen H. Dingley - Schrödinger Inc., New York, New York, 10036, United States

Jeffrey A. Bell - Schrödinger Inc., New York, New York, 10036, United States

Yuansong Jiang - Viva Biotech, Shanghai 201203, China

Hua Zhou - Viva Biotech, Shanghai 201203, China

Robert J. Skene - Takeda California Inc., San Diego, California 92121, United States; orcid.org/0000-0002-1482-6546

ACKNOWLEDGMENTS

ABBREVIATIONS

ADME, Absorption, Distribution, Metabolism and Excretion; ALS, Amyotrophic lateral sclerosis; AUC, Area Under the Curve; BDC, bile duct cannulation; BCS, Biopharmaceutical Classification System; CIPN, Chemotherapy induced peripheral neuropathy; cJUN, Transcription factor Jun; Cl, clearance; CLint, Intrinsic clearance; CNS, central nervous system; CYP3A, cytochrome P450 3A family; DLK, dual leucine zipper; DRG, dorsal root ganglion; Eh, hepatic extraction ratio; ER, efflux ratio; E-sol, Energy of solvation; FEP, free energy perturbation; GSH, Glutathione; hERG, human Ether-a-go-go-Related Gene; hLM, human liver microsomes; IC_{50}: Half-maximal inhibitory concentration; IV, intravenous; K_i, inhibitory constant; $K_{p,uu}$, unbound brain-to-plasma drug partition coefficient; LE, ligand efficiency; logP, partition coefficient; logD, distribution coefficient; LZK, Leucine zipper-bearing kinase; MDCK, Madin-Darby canine kidney;

MDR1, multidrug resistance protein; mLM, mouse liver microsomes; MLK, Mixed lineage kinase; MPO, multi-parameter optimization; MUE, mean unsigned error; NADPH, Nicotinamide adenine dinucleotide phosphate; Papp, apparent permeability; P-gp, P-glycoprotein; p-JNK, phosporylated c-Jun N-terminal kinase; PK, pharmacokinetics; PO, oral administration; QM, quantum mechanics; ROC, Receiver Operating Characteristic; RRCK, Ralph Russ canine kidney; SAR, structure-activity relationships; SEM, standard error of the mean; THP, tetrahydropyran.

REFERENCES

(1) Fukuda, Y.; Li, Y.; Segal, R. A. A Mechanistic Understanding of Axon Degeneration in Chemotherapy-Induced Peripheral Neuropathy. *Front. Neurosci.* **2017**, *11*, 481.

(2) Fan, G.; Merritt, S. E.; Kortenjann, M.; Shaw, P. E.; Holzman, L. B. Dual Leucine Zipper-Bearing Kinase (DLK) Activates p46SAPK and p38mapk but Not ERK2. *J. Biol. Chem.* **1996**, *271* (40), 24788–24793.

(3) Patel, S.; Meilandt, W. J.; Erickson, R. I.; Chen, J.; Deshmukh, G.; Estrada, A. A.; Fuji, R. N.; Gibbons, P.; Gustafson, A.; Harris, S. F.; Imperio, J.; Liu, W.; Liu, X.; Liu, Y.; Lyssikatos, J. P.; Ma, C.; Yin, J.; Lewcock, J. W.; Siu, M. Selective Inhibitors of Dual Leucine Zipper Kinase (DLK, MAP3K12) with Activity in a Model of Alzheimer's Disease. *J. Med. Chem.* **2017**, *60* (19), 8083–8102.

(4) Pichon, C. E. L.; Meilandt, W. J.; Dominguez, S.; Solanoy, H.; Lin, H.; Ngu, H.; Gogineni, A.; Ghosh, A. S.; Jiang, Z.; Lee, S.-H.; Maloney, J.; Gandham, V. D.; Pozniak, C. D.; Wang, B.; Lee, S.; Siu, M.; Patel, S.; Modrusan, Z.; Liu, X.; Rudhard, Y.; Baca, M.; Gustafson, A.; Kaminker, J.; Carano, R. A. D.; Huang, E. J.; Foreman, O.; Weimer, R.; Scearce-Levie, K.; Lewcock, J. W. Loss of Dual Leucine Zipper Kinase Signaling Is Protective in Animal Models of Neurodegenerative Disease. *Sci. Transl. Med.* **2017**, *9* (403), eaag0394.

(5) Craig, R. A., 2nd; Fox, B. M.; Hu, C.; Lexa, K. W.; Osipov, M.; Thottumkara, A. P.; Larhammar, M.; Miyamoto, T.; Rana, A.; Kane, L. A.; Yulyaningsih, E.; Solanoy, H.; Nguyen, H.; Chau, R.; Earr, T.; Kajiwara, Y.; Fleck, D.; Lucas, A.; Haddick, P. C. G.; Takahashi, R. H.; Tong, V.; Wang, J.; Canet, M. J.; Poda, S. B.; Scearce-Levie, K.; Srivastava, A.; Sweeney, Z. K.; Xu, M.; Zhang, R.; He, J.; Lei, Y.; Zhuo, Z.; de Vicente, J. Discovery of Potent and Selective Dual Leucine Zipper Kinase/Leucine Zipper-Bearing Kinase Inhibitors with Neuroprotective Properties in In Vitro and In Vivo Models of Amyotrophic Lateral Sclerosis. *J. Med. Chem.* **2022**, *65* (24), 16290–16312.

(6) Le, K.; Soth, M. J.; Cross, J. B.; Liu, G.; Ray, W. J.; Ma, J.; Goodwani, S. G.; Acton, P. J.; Buggia-Prevot, V.; Akkermans, O.; Barker, J.; Conner, M. L.; Jiang, Y.; Liu, Z.; McEwan, P.; Warner-Schmidt, J.; Xu, A.; Zebisch, M.; Heijnen, C. J.; Abrahams, B.; Jones, P. Discovery of IACS-52825, a Potent and Selective DLK Inhibitor for Treatment of Chemotherapy-Induced Peripheral Neuropathy. *J. Med. Chem.* **2023**, *66* (14), 9954–9971.

(7) Ma, J.; Goodwani, S.; Acton, P. J.; Buggia-Prevot, V.; Kesler, S. R.; Jamal, I.; Mahant, I. D.; Liu, Z.; Mseeh, F.; Roth, B. L.; Chakraborty, C.; Peng, B.; Wu, Q.; Jiang, Y.; Le, K.; Soth, M. J.; Jones, P.; Kavelaars, A.; Ray, W. J.; Heijnen, C. J. Inhibition of Dual Leucine Zipper Kinase Prevents Chemotherapy-Induced Peripheral Neuropathy and Cognitive Impairments. *Pain* **2021**, *162* (10), 2599–2612.

(8) Siu, M.; Sengupta Ghosh, A.; Lewcock, J. W. Dual Leucine Zipper Kinase Inhibitors for the Treatment of Neurodegeneration. *J. Med. Chem.* **2018**, *61* (18), 8078–8087.

(9) Karaman, M. W.; Herrgard, S.; Treiber, D. K.; Gallant, P.; Atteridge, C. E.; Campbell, B. T.; Chan, K. W.; Ciceri, P.; Davis, M. I.; Edeen, P. T.; Faraoni, R.; Floyd, M.; Hunt, J. P.;

Lockhart, D. J.; Milanov, Z. V.; Morrison, M. J.; Pallares, G.; Patel, H. K.; Pritchard, S.; Wodicka, L. M.; Zarrinkar, P. P. A Quantitative Analysis of Kinase Inhibitor Selectivity. *Nat. Biotechnol.* **2008**, *26* (1), 127–132.

(10) Ferraris, D.; Yang, Z.; Welsbie, D. Dual Leucine Zipper Kinase as a Therapeutic Target for Neurodegenerative Conditions. *Future Med. Chem.* **2013**, *5* (16), 1923–1934.

(11) Patel, S.; Cohen, F.; Dean, B. J.; De La Torre, K.; Deshmukh, G.; Estrada, A. A.; Ghosh, A. S.; Gibbons, P.; Gustafson, A.; Huestis, M. P.; Le Pichon, C. E.; Lin, H.; Liu, W.; Liu, X.; Liu, Y.; Ly, C. Q.; Lyssikatos, J. P.; Ma, C.; Scearce-Levie, K.; Shin, Y. G.; Solanoy, H.; Stark, K. L.; Wang, J.; Wang, B.; Zhao, X.; Lewcock, J. W.; Siu, M. Discovery of Dual Leucine Zipper Kinase (DLK, MAP3K12) Inhibitors with Activity in Neurodegeneration Models. *J. Med. Chem.* **2015**, *58* (1), 401–418.

(12) Katz, J. S.; Rothstein, J. D.; Cudkowicz, M. E.; Genge, A.; Oskarsson, B.; Hains, A. B.; Chen, C.; Galanter, J.; Burgess, B. L.; Cho, W.; Kerchner, G. A.; Yeh, F. L.; Ghosh, A. S.; Cheeti, S.; Brooks, L.; Honigberg, L.; Couch, J. A.; Rothenberg, M. E.; Brunstein, F.; Sharma, K. R.; van den Berg, L.; Berry, J. D.; Glass, J. D. A Phase 1 Study of GDC-0134, a Dual Leucine Zipper Kinase Inhibitor, in ALS. *Ann. Clin. Transl. Neurol.* **2022**, *9* (1), 50–66.

(13) Wang, L.; Wu, Y.; Deng, Y.; Kim, B.; Pierce, L.; Krilov, G.; Lupyan, D.; Robinson, S.; Dahlgren, M. K.; Greenwood, J.; Romero, D. L.; Masse, C.; Knight, J. L.; Steinbrecher, T.; Beuming, T.; Damm, W.; Harder, E.; Sherman, W.; Brewer, M.; Wester, R.; Murcko, M.; Frye, L.; Farid, R.; Lin, T.; Mobley, D. L.; Jorgensen, W. L.; Berne, B. J.; Friesner, R. A.; Abel, R. Accurate and Reliable Prediction of Relative Ligand Binding Potency in Prospective Drug Discovery by Way of a Modern Free-Energy Calculation Protocol and Force Field. *J. Am. Chem. Soc.* **2015**, *137* (7), 2695–2703.

(14) Lu, C.; Wu, C.; Ghoreishi, D.; Chen, W.; Wang, L.; Damm, W.; Ross, G. A.; Dahlgren, M. K.; Russell, E.; Von Bargen, C. D.; Abel, R.; Friesner, R. A.; Harder, E. D. OPLS4: Improving Force Field Accuracy on Challenging Regimes of Chemical Space. *J. Chem. Theory Comput.* **2021**, *17* (7), 4291–4300.

(15) Gunaydin, H. Probabilistic Approach to Generating MPOs and Its Application as a Scoring Function for CNS Drugs. *ACS Med. Chem. Lett.* **2016**, *7* (1), 89–93.

(16) Tang, H.; Jensen, K.; Houang, E.; McRobb, F. M.; Bhat, S.; Svensson, M.; Bochevarov, A.; Day, T.; Dahlgren, M. K.; Bell, J. A.; Frye, L.; Skene, R. J.; Lewis, J. H.; Osborne, J. D.; Tierney, J. P.; Gordon, J. A.; Palomero, M. A.; Gallati, C.; Chapman, R. S. L.; Jones, D. R.; Hirst, K. L.; Sephton, M.; Chauhan, A.; Sharpe, A.; Tardia, P.; Dechaux, E. A.; Taylor, A.; Waddell, R. D.; Valentine, A.; Janssens, H. B.; Aziz, O.; Bloomfield, D. E.; Ladha, S.; Fraser, I. J.; Ellard, J. M. Discovery of a Novel Class of D-Amino Acid Oxidase Inhibitors Using the Schrödinger Computational Platform. *J. Med. Chem.* **2022**, *65* (9), 6775–6802.

(17) Johnston, R. C.; Yao, K.; Kaplan, Z.; Chelliah, M.; Leswing, K.; Seekins, S.; Watts, S.; Calkins, D.; Chief Elk, J.; Jerome, S. V.; Repasky, M. P.; Shelley, J. C. Epik: pKa and Protonation State Prediction through Machine Learning. *J. Chem. Theory Comput.* **2023**, *19* (8), 2380–2388.

(18) Larhammar, M.; Huntwork-Rodriguez, S.; Rudhard, Y.; Sengupta-Ghosh, A.; Lewcock, J. W. The Ste20 Family Kinases MAP4K4, MINK1, and TNIK Converge to Regulate Stress-Induced JNK Signaling in Neurons. *J. Neurosci.* **2017**, *37* (46), 11074–11084.

(19) Kalgutkar, A. S.; Obach, R. S.; Maurer, T. S. Mechanism-Based Inactivation of Cytochrome P450 Enzymes: Chemical Mechanisms, Structure-Activity Relationships and Relationship to Clinical Drug-Drug Interactions and Idiosyncratic Adverse Drug Reactions. *Curr. Drug Metab.* **2007**, *8* (5), 407–447.

(20) Hollenberg, P. F.; Kent, U. M.; Bumpus, N. N. Mechanism-Based Inactivation of Human Cytochromes p450s: Experimental Characterization, Reactive Intermediates, and Clinical Implications. *Chem. Res. Toxicol.* **2008**, *21* (1), 189–205.

(21) Kalgutkar, A. S. Designing around Structural Alerts in Drug Discovery. *J. Med. Chem.* **2020**,

63 (12), 6276–6302.

(22) Wager, T. T.; Hou, X.; Verhoest, P. R.; Villalobos, A. Moving beyond Rules: The Development of a Central Nervous System Multiparameter Optimization (CNS MPO) Approach to Enable Alignment of Druglike Properties. *ACS Chem. Neurosci.* **2010**, *1* (6), 435–449.

(23) Loryan, I.; Reichel, A.; Feng, B.; Bundgaard, C.; Shaffer, C.; Kalvass, C.; Bednarczyk, D.; Morrison, D.; Lesuisse, D.; Hoppe, E.; Terstappen, G. C.; Fischer, H.; Di, L.; Colclough, N.; Summerfield, S.; Buckley, S. T.; Maurer, T. S.; Fridén, M. Unbound Brain-to-Plasma Partition Coefficient, $K_{p,uu,brain}$-a Game Changing Parameter for CNS Drug Discovery and Development. *Pharm. Res.* **2022**, *39* (7), 1321–1341.

(24) Hammarlund-Udenaes, M.; Fridén, M.; Syvänen, S.; Gupta, A. On the Rate and Extent of Drug Delivery to the Brain. *Pharm. Res.* **2008**, *25* (8), 1737–1750.

(25) Leung, S. S. F.; Mijalkovic, J.; Borrelli, K.; Jacobson, M. P. Testing Physical Models of Passive Membrane Permeation. *J. Chem. Inf. Model.* **2012**, *52* (6), 1621–1636.

(26) Lawrenz, M.; Svensson, M.; Kato, M.; Dingley, K. H.; Chief Elk, J.; Nie, Z.; Zou, Y.; Kaplan, Z.; Lagiakos, H. R.; Igawa, H.; Therrien, E. A Computational Physics-Based Approach to Predict Unbound Brain-to-Plasma Partition Coefficient, $K_{p,uu}$. *J. Chem. Inf. Model.* **2023**, *63* (12), 3786–3798.

(27) Goodwani, S.; Fernandez, C.; Acton, P. J.; Buggia-Prevot, V.; McReynolds, M. L.; Ma, J.; Hu, C. H.; Hamby, M. E.; Jiang, Y.; Le, K.; Soth, M. J.; Jones, P.; Ray, W. J. Dual Leucine Zipper Kinase Is Constitutively Active in the Adult Mouse Brain and Has Both Stress-Induced and Homeostatic Functions. *Int. J. Mol. Sci.* **2020**, *21* (14). https://doi.org/10.3390/ijms21144849.

(28) Fong, K. L.; Hwang, B. Y. Dog Liver N-Methyltransferase. A Drug-Metabolizing Enzyme. *Biochem. Pharmacol.* **1983**, *32* (18), 2781–2786.

(29) *Schrödinger Release 2021-4: Jaguar, Schrödinger, LLC, New York, NY, 2021*. https://www.schrodinger.com/platform/products/jaguar/ (accessed 2024-05-29).

(30) *Schrödinger Release 2021-4: FEP+, Schrödinger, LLC, New York, NY, 2021*. https://www.schrodinger.com/platform/products/fep/ (accessed 2024-05-29).

(31) *Schrödinger Release 2021-4: Prime, Schrödinger, LLC, New York, NY, 2021*. https://www.schrodinger.com/platform/products/prime/ (accessed 2024-05-29).

(32) *Schrödinger Release 2021-4: LiveDesign, Schrödinger, LLC, New York, NY, 2021*. Schrodinger. https://www.schrodinger.com/platform/products/livedesign/ (accessed 2024-05-29).

(33) *RDKit*. http://www.rdkit.org/.

(34) *Schrödinger Release 2021-4: Epik, Schrödinger, LLC, New York, NY, 2021*. https://www.schrodinger.com/platform/products/epik/ (accessed 2024-05-29).

(35) Johnson, S. A. *Probabilistic Multi-Parameter Optimization (pMPO)*. https://github.com/Merck/pmpo (accessed 2022-10-24).